Inorganic Chemistry

pubs.acs.org/IC

Article

Unravelling the Mechanism of Excited-State Interligand Energy Transfer and the Engineering of Dual Emission in $[Ir(C^N)_2(N^N)]^+$ Complexes

Paul A. Scattergood,* Anna M. Ranieri, Luke Charalambou, Adrian Comia, Daniel A. W. Ross, Craig R. Rice, Samantha J. O. Hardman, Jean-Louis Heully, Isabelle M. Dixon, Massimiliano Massi, Fabienne Alary,* and Paul I. P. Elliott*

Cite This: https://dx.doi.org/10.1021/acs.inorgchem.9b03003

Read Online

ACCESS | Metrics & More | Article Recommendations | Supporting Information

ABSTRACT: Fundamental insights into the mechanism of triplet-excited-state interligand energy transfer dynamics and the origin of dual emission for phosphorescent iridium(III) complexes are presented. The complexes $[Ir(C^N)_2(N^N)]^+$ (HC^N = 2-phenylpyridine (**1a**–**c**), 2-(2,4-difluorophenyl)pyridine (**2a**–**c**), 1-benzyl-4-phenyl-1,2,3-triazole (**3a**–**c**); N^N = 1-benzyl-4-(pyrid-2-yl)-1,2,3-triazole (pytz, **a**), 1-benzyl-4-(pyrimidin-2-yl)-1,2,3-triazole (pymtz, **b**), 1-benzyl-4-(pyrazin-2-yl)-1,2,3-triazole (pyztz, **c**)) are phosphorescent in room-temperature fluid solutions from triplet metal-to-ligand charge transfer (^{3}MLCT) states admixed with either ligand-centered (^{3}LC) (**1a**, **2a**, and **2b**) or ligand-to-ligand charge transfer (^{3}LL′CT) character (**1c**, **2c**, and **3a**–**c**). Particularly striking is the observation that pyrimidine-based complex **1b** exhibits dual emission from both ^{3}MLCT/^{3}LC and ^{3}MLCT/^{3}LL′CT states. At 77 K, the ^{3}MLCT/^{3}LL′CT component is lost from the photoluminescence spectra of **1b**, with emission exclusively arising from its ^{3}MLCT/^{3}LC state, while for **2c** switching from ^{3}MLCT/^{3}LL′CT- to ^{3}MLCT/^{3}LC-based emission is observed. Femtosecond transient absorption data reveal distinct spectral signatures characteristic of the population of ^{3}MLCT/^{3}LC states for **1a**, **2a**, and **2b** which persist throughout the 3 ns time frame of the experiment. These ^{3}MLCT/^{3}LC state signatures are apparent in the transient absorption spectra for **1c** and **2c** immediately following photoexcitation but rapidly evolve to yield spectral profiles characteristic of their ^{3}MLCT/^{3}LL′CT states. Transient data for **1b** reveals intermediate behavior: the spectral features of the initially populated ^{3}MLCT/^{3}LC state also undergo rapid evolution, although to a lesser extent than that observed for **1c** and **2c**, behavior assigned to the equilibration of the ^{3}MLCT/^{3}LC and ^{3}MLCT/^{3}LL′CT states. Density functional theory (DFT) calculations enabled minima to be optimized for both ^{3}MLCT/^{3}LC and ^{3}MLCT/^{3}LL′CT states of **1a**–**c** and **2a**–**c**. Indeed, two distinct ^{3}MLCT/^{3}LC minima were optimized for **1a**, **1b**, **2a**, and **2b** distinguished by upon which of the two C^N ligands the excited electron resides. The ^{3}MLCT/^{3}LC and ^{3}MLCT/^{3}LL′CT states for **1b** are very close in energy, in excellent agreement with experimental data demonstrating dual emission. Calculated vibrationally resolved emission spectra (VRES) for the complexes are in excellent agreement with experimental data, with the overlay of spectral maxima arising from emission from the ^{3}MLCT/^{3}LC and ^{3}MLCT/^{3}LL′CT states of **1b** convincingly reproducing the observed experimental spectral features. Analysis of the optimized excited-state geometries enable the key structural differences between the ^{3}MLCT/^{3}LC and ^{3}MLCT/^{3}LL′CT states of the complexes to be identified and quantified. The calculation of interconversion pathways between triplet excited states provides for the first time a through-space mechanism for a photoinduced interligand energy transfer process. Furthermore, examination of structural changes between the possible emitting triplet excited states reveals the key bond vibrations that mediate energy transfer between these states. This work therefore provides for the first time detailed mechanistic insights into the fundamental photophysical processes of this important class of complexes.

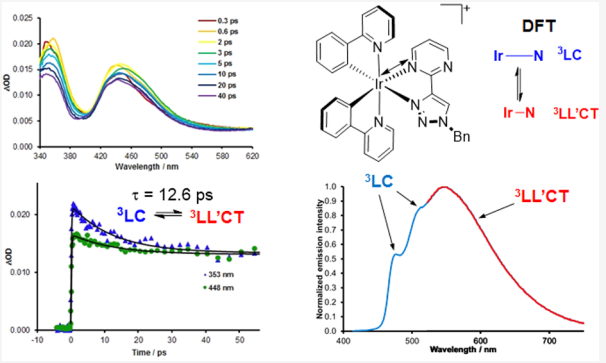

INTRODUCTION

Cyclometalated iridium(III) complexes based on the archetypal complexes $[Ir(ppy)_3]$ and $[Ir(ppy)_2(bpy)]^+$ (ppyH = 2-phenylpyridine; bpy = 2,2′-bipyridyl) form one of the cornerstones of modern transition metal photochemistry. Typified by their efficient phosphorescence,[1,2] structural

Received: October 11, 2019

modification of the ligands yields luminescence with perceived color tunability throughout the visible spectrum leading to extensive investigations for the application of these complexes in phosphorescent organic light-emitting diode (PhOLED)[3] and light-emitting electrochemical cell (LEC) devices,[4−6] as luminescent biological probes for confocal microscopy[7−12] and as luminescent sensors.[13,14] The properties of their triplet excited states also lend themselves to applications in photodynamic therapy[15−17] and as sensitizers in photocatalysis.[18−22]

For heteroleptic complexes with the general structure $[Ir(C^N)_2(N^N)]^+$, phosphorescence can derive from excited states localized on either the neutral ancillary N^N ligand or the anionic cyclometalated C^N ligands.[23] The highest occupied molecular orbital (HOMO) for these cationic heteroleptic complexes typically has contributions from an Ir d-orbital as well as from the π-system of the aryl rings of the C^N ligands, while the lowest unoccupied molecular orbital (LUMO) has primarily π^*-character localized on the ancillary N^N ligand. Thus, the observed emission from these complexes generally derives from triplet metal-to-ligand charge transfer (^{3}MLCT) states admixed with ligand-to-ligand charge transfer (ancillary-based, ^{3}LL′CT) or alternatively ligand-centered (^{3}LC) state character through population of higher lying vacant C^N-based orbitals. The nature of the emitting state can typically be inferred from the band shape, with broad featureless emission bands observed for ^{3}MLCT/^{3}LL′CT state phosphorescence while structured emission bands exhibiting vibronic progressions result from ^{3}MLCT/^{3}LC states.[23−27] Upon photoexcitation, the complex $[Ir(ppy)_2(bpy)]^+$ exhibits a broad featureless emission band that derives from a ^{3}MLCT/^{3}LL′CT state of HOMO → LUMO character. For the fluorinated complex $[Ir(dfppy)_2(bpy)]^+$ (dfppyH = 2-(2,4-difluorophenyl)pyridine), the room-temperature emission spectrum is of similar ^{3}MLCT/^{3}LL′CT character; however, the spectrum at 77 K becomes highly structured, indicative of a change from ^{3}MLCT/^{3}LL′CT- to ^{3}MLCT/^{3}LC-derived luminescence upon cooling. Ultrafast transient absorption[28] and emission upconversion[29] data for these and related complexes reveal an initially populated ^{3}MLCT/^{3}LC state followed by population transfer to the ^{3}MLCT/^{3}LL′CT state occurring on a picosecond time scale after photoexcitation. Replacement of the bpy ancillary N^N ligand by pytz (4-(pyrid-2-yl)-1,2,3-triazole) in the complexes $[Ir(ppy)_2(pytz)]^+$ and $[Ir(dfppy)_2(pytz)]^+$ results in ^{3}MLCT/^{3}LC-based emission in room-temperature solutions[30] despite the LUMO in each case still being localized on the N^N ligand, albeit being heavily destabilized with respect to those of their bpy-containing analogues.[31] Thus, the nature of the N^N and C^N ligands and their influence on the topology of the triplet-excited-state potential energy surface leads to fundamental differences in the excited-state dynamics and the resultant steady-state emission character. Despite the clear importance of this class of compound and the mass of data collected in recent years, the exact structure/property relationships that determine the ultimate emitting state or define the reaction coordinate for the observed energy transfer between excited states remain unclear.

For this contribution, we set out to formulate a series of complexes through which a comprehensive spectroscopic and computational density functional theory investigation would enable fundamental additional insights into the excited-state dynamics of cyclometalated iridium(III) complexes to be obtained. The series of complexes depicted in Figure 1 was designed around a three-pronged strategy to yield effective and

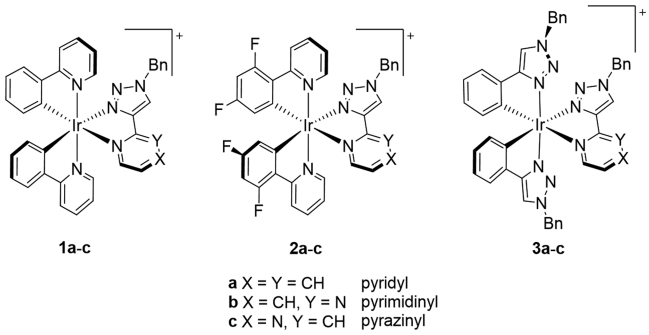

Figure 1. Structures of complexes **1a−c**, **2a−c**, and **3a−c**.

selective tuning of different excited states and the ground state as outlined below:

(i) First, variation of the ancillary N^N ligand will enable selective tuning of the energy of the ^{3}MLCT/^{3}LL′CT state with an anticipated minimal impact on the C^N-based ^{3}MLCT/^{3}LC state. While the known complexes $[Ir(ppy)_2(pytz)]^+$ (**1a**) and $[Ir(dfppy)_2(pytz)]^+$ (**2a**) exhibit ^{3}MLCT/^{3}LC-based emission[30] despite possessing a pytz π^*-based LUMO, ancillary ligands such as 2,2′-bipyrazine are known to be more electron withdrawing and have a lower energy LUMO than bpy which will promote ^{3}LL′CT-based emission. We therefore designed analogous ancillary ligands to pytz (**a**) containing progressively more electron withdrawing pyrimidine (pymtz, **b**) and pyrazine (pyztz, **c**) rings in place of pyridine. We were confident that this would then achieve efficient tuning of the LUMO of their resultant complexes, enabling a deliberate spanning of ^{3}MLCT/^{3}LC and ^{3}MLCT/^{3}LL′CT emission regimes. Three series of complexes were then envisaged based on these three triazole-based ancillary ligands with additional variation in the C^N ligands. The minimal structural variation for the largely isostructural complexes within each of the three sets thereby removes potential interpretative complications in our photophysical results.

(ii) Fluorination of the aryl rings of the C^N ligands (as in the dfppy-based complexes **2a−c**) stabilizes the HOMO leading to an apparent *destabilization* of emissive excited states compared to analogous ppy-based complexes (**1a−c**) and consequential blue-shifted luminescence. In addition, the two potential emissive states of different character (^{3}MLCT/^{3}LC and ^{3}MLCT/^{3}LL′CT) are anticipated to be perturbed to differing degrees, leading to an intended subtle tuning on relative excited-state energies between ppy- and dfppy-containing series.

(iii) The third set of complexes **3a−c** incorporate phenyltriazole-based (ptz) C^N ligands with replacement of the ppy pyridine ring in **1a−c** by a 1,2,3-triazole moiety. Since the triazole-based unoccupied orbitals will be significantly destabilized with respect to those for ppy-based pyridine moieties, complexes **3a−c** were designed in order to destabilize the ^{3}MLCT/^{3}LC states relative to the ^{3}MLCT/^{3}LL′CT state, enabling the

https://dx.doi.org/10.1021/acs.inorgchem.9b03003
Inorg. Chem. XXXX, XXX, XXX−XXX

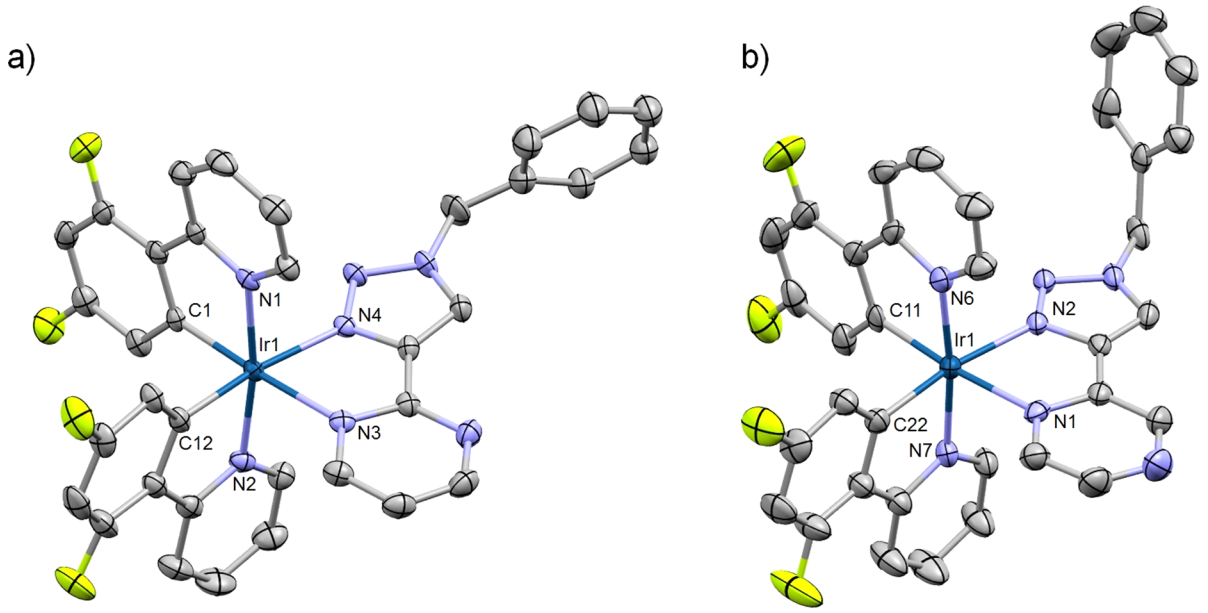

Figure 2. Molecular structures of complexes **2b** (a) and **2c** (b). Thermal ellipsoids are shown at 50% probability with hydrogen atoms, cocrystallized solvent molecules, and hexafluorophosphate counterions removed for clarity. Bond lengths (Å) and angles (deg): **2b**: Ir(1)−N(1) = 2.046(3), Ir(1)−C(1) = 2.008(3), Ir(1)−N(2) = 2.043(3), Ir(1)−C(12) = 1.999(4), Ir(1)−N(3) = 2.159(3), Ir(1)−N(4) = 2.137(3), N(1)−Ir(1)−C(1) = 80.42, N(2)−Ir(1)−C(12) = 80.59, N(3)−Ir(1)−N(4) = 76.14, N(1)−Ir(1)−N(2) = 170.99, C(1)−Ir(1)−N(3) = 176.41, N(4)−Ir(1)−C(12) = 170.88 (CCDC 1953486). **2c**: Ir(1)−N(1) = 2.159(3), Ir(1)−N(2) = 2.125(3), Ir(1)−N(6) = 2.055(3), Ir(1)−C(11) = 2.006(4), Ir(1)−N(7) = 2.046(3), Ir(1)−C(22) = 2.004(4), N(1)−Ir(1)−N(2) = 76.41, N(6)−Ir(1)−C(11) = 80.27, N(7)−Ir(1)−C(22) = 80.33, N(1)−Ir(1)−C(11) = 174.45, N(2)−Ir(1)−C(22) = 171.45, N(6)−Ir(1)−N(7) = 173.25 (CCDC 1953487).

^{3}MLCT/^{3}LL′CT state to be studied in isolation, at least in fluid solution.[32,33]

Kasha's rule states that emission from a luminophore will occur from the lowest lying excited state of a given spin multiplicity. However, through careful tuning of the relative energies of the ^{3}MLCT/^{3}LL′CT and ^{3}MLCT/^{3}LC states such that they are, or are approximately isoenergetic, dual emission character will be possible. Importantly, we show here that through this strategy room temperature dual emission from both ^{3}MLCT-based states has indeed been realized. In an attempt to understand, and later to identify some criteria favoring dual emission and processes underpinning interligand energy transfer, we first examined the ground-state molecular orbital diagrams, which brought some interesting insights especially in the LUMO−LUMO+2 region. Further information was provided by optimizing the lowest triplet excited states where close examination of their geometries revealed subtle differences. Depending on the ligand set, one, two or three distinct and potentially emissive excited-state minima were identified for the complexes, and their vibrationally resolved emission spectra were modeled, in perfect agreement with experimental emission energies and bandshapes. The minimum energy paths connecting the ^{3}MLCT/^{3}LC and ^{3}MLCT/^{3}LL′CT states were also computed for selected complexes. The absence of gradual orbital mixing and metal-mediated electronic communication along these paths leads us to discuss on the mechanism for triplet−triplet state interconversion in these systems. Key vibrations were subsequently searched for, and identified, that favor the transfer from the initially populated ^{3}MLCT/^{3}LC state to the ^{3}MLCT/^{3}LL′CT state. Altogether, the complete set of experimental and theoretical data allows us to propose a full rationalization of room temperature and low temperature emission data, as well as some insights into the factors that favor dual emission (subtle geometry changes and promoting vibrational modes).

RESULTS AND DISCUSSION

Synthesis and Characterization. The new ligands pymtz and pyztz were prepared through copper(I)-catalyzed alkyne−azide cycloaddition of benzyl azide and the corresponding 2-ethynyl-substituted azine (synthetic descriptions, NMR and mass spectral characterization data for pymtz and pyztz ligands are provided in Figures S1−S4). Complexes **1a−c**, **2a−c**, and **3a−c** were prepared via existing protocols from the corresponding chloro-bridged Ir(III) dimers. Briefly, [{Ir(ppy)$_2$Cl}$_2$], [{Ir(dfppy)$_2$Cl}$_2$] or [{Ir(ptz)$_2$Cl}$_2$] was combined with 2 equiv of the appropriate triazole-containing ligand in refluxing $CHCl_3$/MeOH, after which treatment with aqueous NH_4PF_6 yielded the target complexes as their yellow-colored hexafluorophosphate salts (see Figures S5−S25 showing the NMR and mass spectral characterization of the complexes).

Crystals of X-ray diffraction quality were obtained for **2b** and **2c** with the molecular structure of the cations being shown in Figure 2. **2b** crystallizes in the P-1 space group, exhibiting N(1)−Ir(1)−C(1) and N(2)−Ir(I)−C(12) chelate angles of 80.42° and 80.59° for the two cyclometalated ligands respectively, resulting in a distorted octahedral coordination environment. The bite angle with the triazole-pyrimidine ligand is smaller, with N(3)−Ir(1)−N(4) measured at 76.14°. The bond lengths between the iridium center and the cyclometalated carbon atoms are typical for complexes of this type (Ir(1)−C(1) = 2.008 Å, Ir(1)−C(12) = 1.999 Å), being slightly shorter than those to the pyridyl nitrogen atom on the same ligand (Ir(1)−N(1) = 2.046 Å, Ir(1)−N(2) = 2.043 Å). By comparison, the triazole-pyrimidine ligand shows

https://dx.doi.org/10.1021/acs.inorgchem.9b03003
Inorg. Chem. XXXX, XXX, XXX−XXX

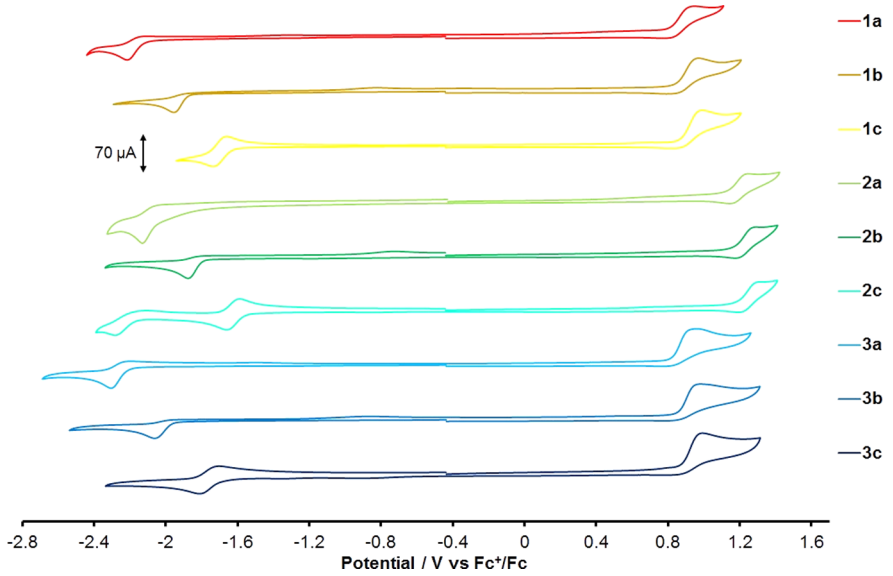

Figure 3. Cyclic voltammograms recorded for 1.6 mmol dm^{-3} MeCN solutions of **1a−3c** at r.t. at 100 mV s^{-1}. Solutions contained 0.2 mol dm^{-3} NBu_4PF_6 as supporting electrolyte. Potentials are shown against the Fc^+/Fc couple.

longer nitrogen−metal bond lengths, with Ir(1)−N(3) and Ir(1)−N(4) being 2.159 and 2.137 Å respectively. The torsion angle between the planes of the pyrimidine and triazole rings is 8.9°, illustrating that the two coordinated heterocycles remain almost coplanar as in the structure of the free ligand, Figure S26). The complex **2c** crystallizes in the P21/c space group along with one molecule of diisopropylether per iridium center. The structure is largely comparable to that of **2b**, with the triazole-pyrazine ligand having a chelate angle N(1)−Ir(1)−N(2) of 76.41°. The bond length between the metal center and the pyrazinyl nitrogen atom is identical to that observed in the pyrimidine analogue (Ir(1)−N(1) = 2.159 Å), while the bond length to the triazole moiety is marginally reduced in **2c** (Ir(1)−N(2) = 2.125 Å).

Electrochemical Characterization. Cyclic voltammograms recorded for all Ir(III) complexes **1a−3c** are shown in Figure 3 with summarized electrochemical data presented in Table 1. Complexes **1a−c** exhibit one irreversible oxidation process in the region of +0.98 V which remains unperturbed with variation of the ancillary ligand. This electrochemical behavior is similar to that observed for several other ppy-containing Ir(III) complexes and is attributed to removal of an electron from the highest occupied molecular orbital (HOMO) which is largely localized over the cyclometalated phenyl rings and the Ir center. This assignment is further supported by the observed anodic shift in oxidation potential to approximately +1.25 V upon inclusion of electron-withdrawing fluorine substituents on the phenyl rings in **2a-2c**, consistent with a decrease in electron density and subsequent stabilization of the HOMO. The oxidation potential recorded for **3a−c**, featuring cyclometalated phenyl-triazole ligands, reverts to approximately +0.98 V, being comparable to that measured for **1a−c** and indicating a largely iridium-cyclometalate-based process, seemingly unperturbed by the exchange of the N-donor fragment of the C^N ligand.

Table 1. Summarized Electrochemical Data for 1.6 mmol dm^{-3} MeCN Solutions of 1a−3c Measured at r.t. at 100 mV s^{-1}[a]

complex	oxidation/V	reduction/V
1a	+0.96	−2.18
1b	+0.98	−1.95
1c	+0.99	−1.70 (80)
2a	+1.25	−2.10
2b	+1.29	−1.88
2c	+1.31	−1.62 (69), −2.20
3a	+0.96	−2.27
3b	+0.99	−2.07
3c	+0.99	−1.76 (118)

[a]Potentials are shown in V vs Fc^+/Fc. For reversible couples $E_{1/2}$ is quoted, with the anodic-cathodic peak separation shown in mV within brackets ($\Delta E_{a,c}$ for Fc^+/Fc was typically 75 mV).

Complex **1a** displays one quasi-reversible reduction process with a peak potential of −2.18 V assigned to reduction of the pyridine moiety within the pyridyl-triazole ligand. The reduction process measured for **1b** is shifted by 230 mV to more positive potential and is found to be irreversible, consistent with a pyrimidine-based reduction. By contrast reduction of the pyrazine moiety in **1c** is represented by the fully reversible redox couple observed at −1.70 V, further shifted to more positive potential relative to that of **1b**. Further reduction processes associated with the cyclometalating ligands were not observed for these complexes within the available solvent window. Directly analogous reduction behavior is observed for the series **2a−c** and **3a−c**, although with marginally more anodic potentials noted for **2a-2c**, likely due to the more electron deficient metal center (*vide supra*) withdrawing electron density from the ancillary ligand. In summary, variation in the energy of the LUMO within these complexes can be readily achieved through careful choice of the heterocycle within the triazole-containing ancillary ligand, with the incorporation of a pyrazine fragment resulting in a significant decrease in the HOMO−LUMO energy gap.

Photophysical Properties: Absorption Spectra. All complexes **1a−3c** display UV−visible absorption spectra in acetonitrile solutions typical for biscyclometalated iridium(III) complexes (Figure 4a). Summarized photophysical data are provided in Table 2. Intense bands higher in energy than 300

https://dx.doi.org/10.1021/acs.inorgchem.9b03003
Inorg. Chem. XXXX, XXX, XXX−XXX

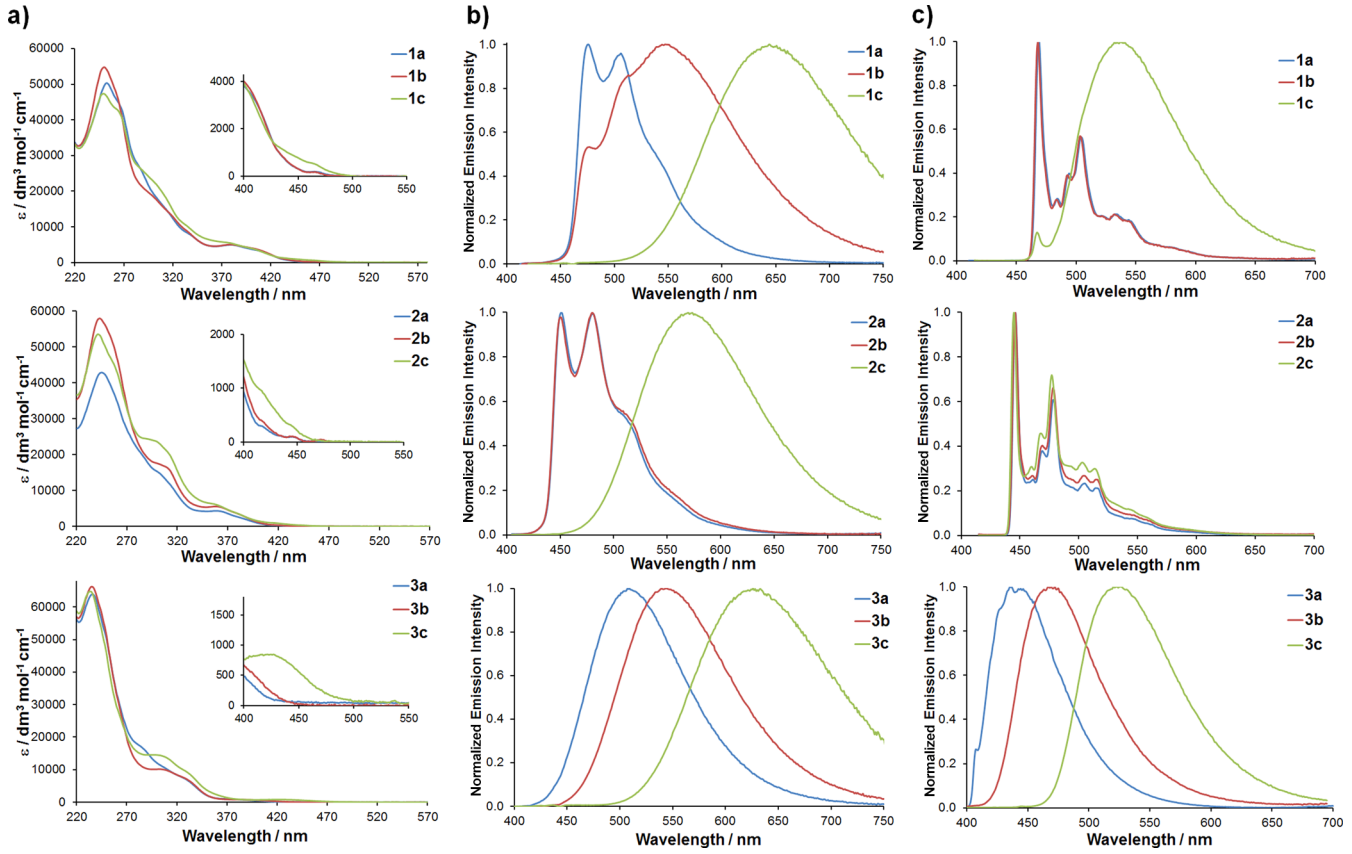

Figure 4. (a) UV−visible electronic absorption spectra recorded for MeCN solutions of **1a−3c**. (b) Emission spectra for **1a−3c** in aerated MeCN solution at r.t. (c) Low-temperature (77 K) emission spectra recorded for **1a−3c** in a glass (4:1 EtOH/MeOH).

Table 2. Summarized Photophysical Data for 1a−3c

	λ_{abs}/nm[a]		λ_{em}/nm[a]	aerated τ/ns[a]	aerated Φ/%[a,c]	degassed τ/ns[b]	degassed Φ/%[b,c]	$k_r(10^5)/s^{-1}$ air[a] (degassed)[b]	$k_{nr}(10^7)/s^{-1}$ air[a] (degassed)[b]
1a	410, 381, 339, 313, 287, 266	R.T.	475, 506, 540 (sh)[f]	58	0.9	2107	34.1	1.55 (1.61)	1.70 (0.031)
		77 K[d]	469, 504, 532[e]						
1b	408, 380, 335, 300, 261	R.T.	474, 514, 547[f]	45	1.2	292	6.4	2.66 (2.19)	2.19 (0.32)
		77 K[d]	468, 503, 531[e]						
1c	463, 405, 376, 334, 302, 264	R.T.	644[f]	62	1.4	175	4.2	2.25 (2.40)	1.59 (0.54)
		77 K[d]	467, 535						
2a	380, 362, 302	R.T.	452, 480, 511(sh)[g]	143	1.2	1850	23.9	0.84 (1.29)	0.69 (0.041)
		77 K[d]	446, 478, 502[e]						
2b	380, 362, 311	R.T.	450, 479, 513(sh)[g]	70	0.6	112 (89%) 232 (11%)	1.0	0.85 (0.89)	1.42 (0.88)
		77 K[d]	447, 479, 504[e]						
2c	418, 381, 355, 312, 298	R.T.	570[g]	104 (52%) 129 (48%)	3.2	1317	38.8	2.48 (2.94)	0.75 (0.046)
		77 K[d]	445, 477, 502[e]						
3a	384, 329, 304, 283	R.T.	508[h]	21	0.7	38	1.6	3.33 (4.21)	4.72 (2.59)
		77 K[d]	439						
3b	384, 329, 305	R.T.	544[h]	48	1.5	648	18.7	3.12 (2.88)	2.05 (0.12)
		77 K[d]	466						
3c	430, 332, 304	R.T.	626[h]	83	1.9	341	7.7	2.29 (2.25)	1.18 (0.27)
		77 K[d]	520						

[a]Aerated MeCN. [b]Degassed MeCN. [c]Relative to $[Ru(bpy)_3][PF_6]_2$ Φ = 0.018 in aerated MeCN.[34] [d]4:1 EtOH/MeOH glass. [e]Major vibrational progressions. [f]λ_{ex} = 400 nm. [g]λ_{ex} = 390 nm. [h]λ_{ex} = 385 nm.

nm are assigned as deriving primarily from ligand-centered $\pi \rightarrow \pi^*$ transitions with those lower in energy than 300 nm arising from excitations to singlet metal-to-ligand charge transfer (^{1}MLCT) states, with the weak low energy tail to these absorption bands attributed to direct spin-forbidden transitions to triplet metal-to-ligand charge transfer (^{3}MLCT)

https://dx.doi.org/10.1021/acs.inorgchem.9b03003
Inorg. Chem. XXXX, XXX, XXX−XXX

states. The ppy-based complexes **1a−c** exhibit the lowest energy absorption profiles, with those of the ptz-based complexes **3a−c** showing the highest energy absorption profiles. Within each series the absorption profiles of the pyrazine-based complexes (**c**) are subtly red-shifted compared with those containing pyridyl- (**a**) and pyrimidinyl- (**b**) triazole-based analogues.

Photophysical Properties: Emission Spectra. All complexes are emissive and spectra for each were recorded in room temperature MeCN solutions and at 77 K in ethanol/methanol glass matrices (Figure 4b-c and Table 2). The combination of the effect of the change in both cyclometalated and ancillary ligands in these complexes gives rise to significant tuning of emission color as can be seen from the CIE 1931 chromaticity coordinates depicted in Figure 5, ranging from the sky blue for **2a** to the red/orange for **1c**.

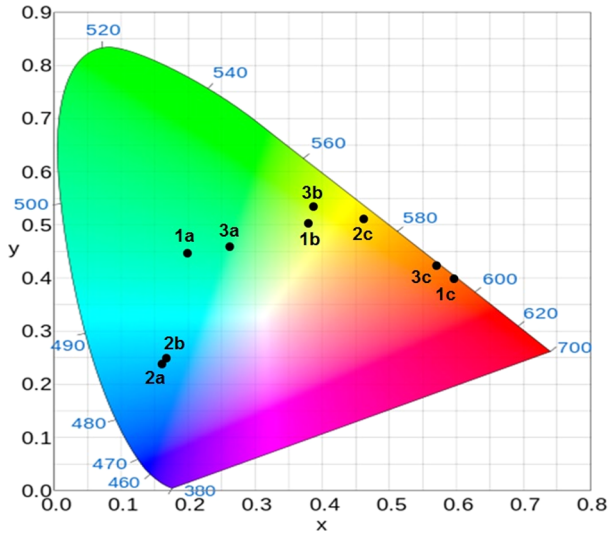

Figure 5. Commission Internationale de l'Éclairage 1931 (CIE) coordinates derived from room-temperature solution-state emission spectra of complexes **1a−3c** in acetonitrile.

The 77 K and room temperature emission spectra for the phenyltriazole-based complexes **3a−c** all show broad featureless emission bands, as expected and indicative of ^{3}MLCT/^{3}LL′CT-based emitting state character. The higher energy of the triazole-based unoccupied molecular orbitals associated with the ptz ligands in **3a−c** compared to the pyridine-based unoccupied orbitals associated with the ppy ligands in **1a−c** ensures that the ^{3}MLCT/^{3}LC states of the former are heavily destabilized. This will favor population of the ^{3}MLCT/^{3}LL′CT states for **3a−c**, whose energies can be considered to be somewhat independent of the N-donor moiety of the cyclometalated ligands providing convenient comparisons to **1a−c**. The emission spectra undergo a red-shift in the energetic ordering pytz > pymtz > pyztz (**a** > **b** > **c**), both at RT and 77 K, in agreement with the progressively stabilized LUMO evident from electrochemical data. These bands show a significant rigidochromic blue-shift when recorded for glass matrices at 77 K compared to their room-temperature spectra in acetonitrile.

Interestingly, the photoluminescence characteristics for **1c** and **2c** are different from those of **1a**, **2a** and **2b** and show different temperature dependence to each other; the room temperature spectra of the former pair in acetonitrile feature broad and unstructured emission bands indicative of ^{3}MLCT/^{3}LL′CT character, while **1a**, **2a** and **2b** all exhibit bands with vibronic progressions characteristic of ^{3}MLCT/^{3}LC emitting states. The emission bands for **2a** and **2b** are near superimposable demonstrating emission from the same state which is independent of the ancillary N^N ligand. The emission profiles of **2a**/**b** and **2c** relative to those of **1a** and **1c**, respectively, are blue-shifted due the stabilization of the HOMO in the dfppy series compared to those ppy-containing complexes due to the electron-withdrawing fluorine substituents, again in agreement with electrochemical and optical absorption data.

Complex **1b** displays a unique and highly intriguing emission behavior. The room temperature emission spectrum recorded for an acetonitrile solution appears to show an emission profile

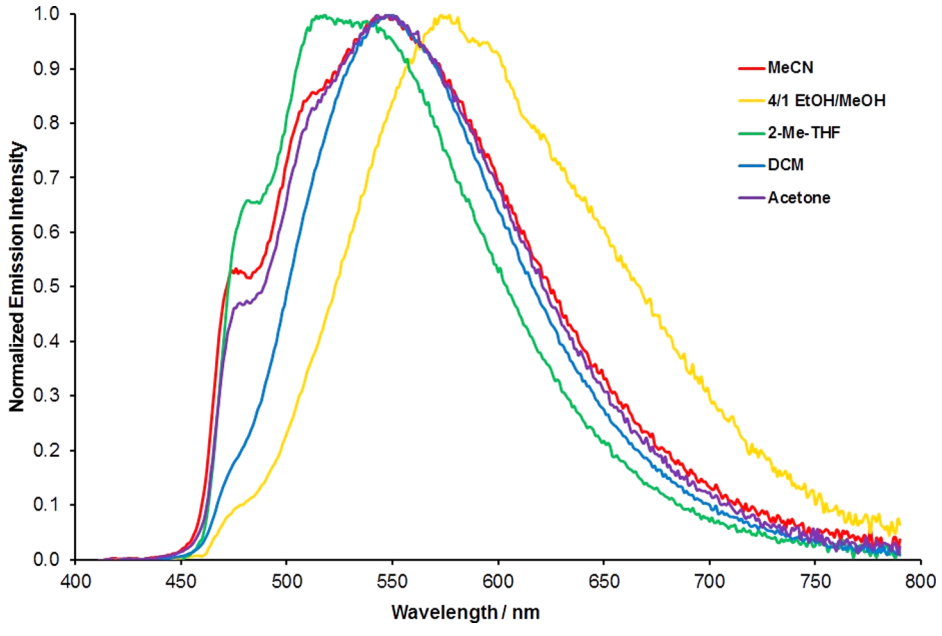

Figure 6. Normalized solvent-dependent emission spectra for **1b** at room temperature.

https://dx.doi.org/10.1021/acs.inorgchem.9b03003
Inorg. Chem. XXXX, XXX, XXX−XXX

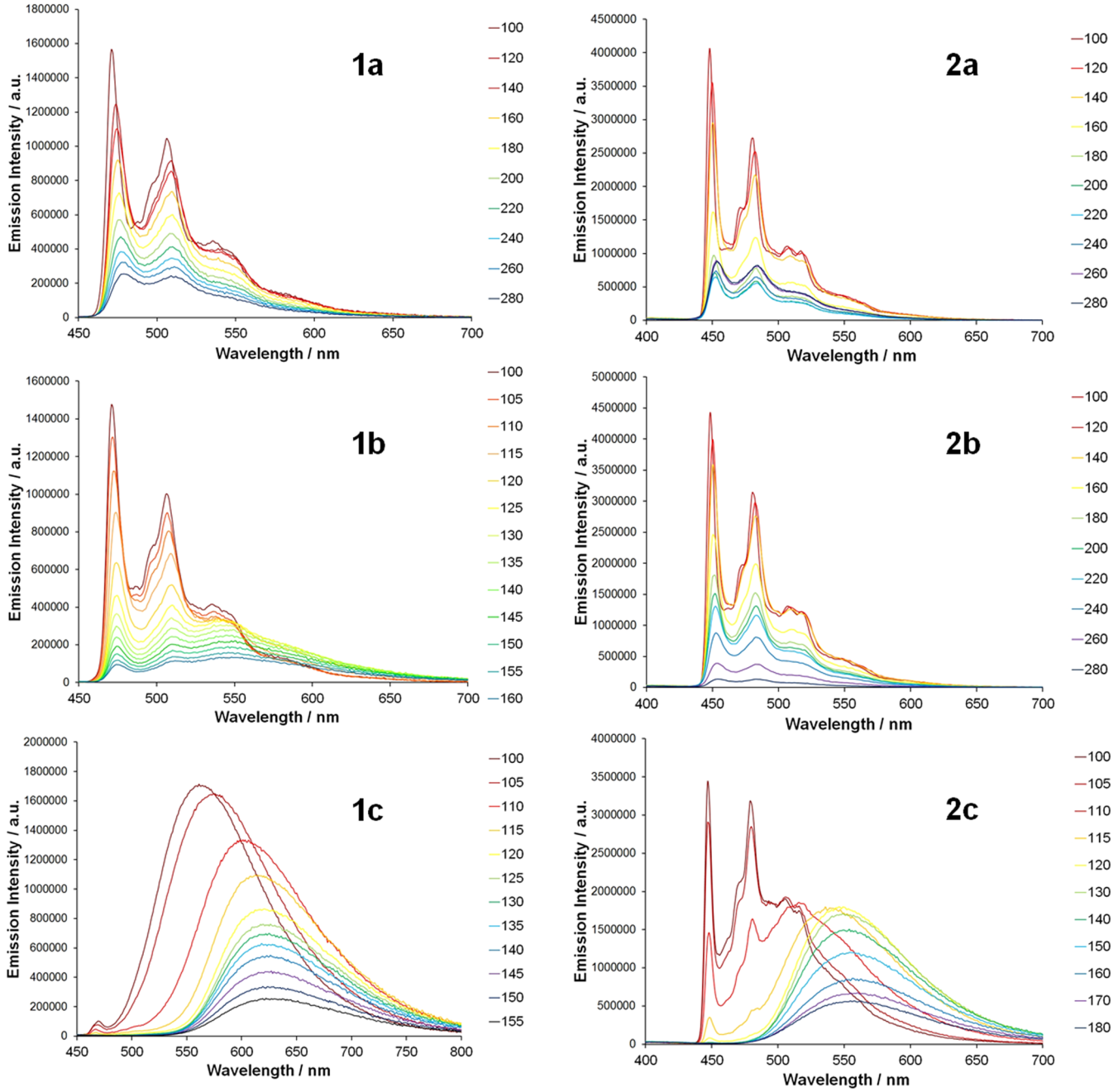

Figure 7. Variable-temperature emission spectra recorded for **1a**−**2c** in 2-Me-THF (m.p. = 137 K). Plots show selected emission profiles at increasing temperature intervals starting from 100 K.

exhibiting both (i) vibronic progressions on the high energy side and (ii) a broad envelope on the low energy side (Figure 4b). It is should be noted that (i) coincide with ^{3}MLCT/^{3}LC progressions in the spectrum for **1a**, while (ii) coincides with the maximum for the emission band of **3b**, indicating that this latter component to the photoluminescence spectrum originates from emission from a ^{3}MLCT/^{3}LL′CT state. Further, excitation spectra recorded at several wavelengths across the spectrum are near identical (Figure S27), all of which closely match the electronic absorption profile, indicative of a unique emitting species. We therefore ascribe the emission profile for **1b** as arising from dual emission from both ^{3}MLCT/^{3}LL′CT and ^{3}MLCT/^{3}LC states. In agreement with the assignment of dual emission from **1b**, the emission profile exhibits solvent dependent variation on the relative intensities of the ^{3}MLCT/^{3}LC and ^{3}MLCT′/^{3}LL′CT-based features (Figure 6). The higher energy ^{3}MLCT/^{3}LC progressions are readily apparent in 2-methyltetrahydrofuran, acetonitrile and acetone solutions but are weaker yet still observable in dichloromethane and in 4:1 ethanol/methanol. The lower energy dominant ^{3}MLCT/^{3}LL′CT-based emission feature is observed to red-shift in this latter solvent system relative to that observed in acetonitrile. This is tentatively assigned as arising from hydrogen bonding between the solvent and the noncoordinated N atom of the pyrimidine ring.

As is commonly observed for biscyclometalated arylpyridine-type complexes,[33] the low temperature emission spectra of **1a**, **2a** and **2b** exhibit much sharper vibronic progressions for the

https://dx.doi.org/10.1021/acs.inorgchem.9b03003
Inorg. Chem. XXXX, XXX, XXX−XXX

^{3}MLCT/^{3}LC emitting state. Interestingly, while a broad featureless emission band indicative of ^{3}MLCT/^{3}LL′CT-derived luminescence is maintained as the dominant feature in the emission spectrum of **1c** at 77 K, the emission profile of **2c** is almost identical to those of **2a** and **2b** indicating switching in the nature of the emissive state to ^{3}MLCT/^{3}LC character at low temperature. For **1b** the low energy envelope assigned to ^{3}MLCT/^{3}LL′CT emission at room temperature is absent at 77 K with the emission profile being almost identical to the ^{3}MLCT/^{3}LC-based emission profile for **1a**, indicating a turning off of dual emission in the low temperature rigid matrix.

Close examination of the 77 K emission spectrum of **1c** reveals a small peak on the high energy side of the emission profile (467 nm), which is almost coincident with the highest energy $\nu_{0\rightarrow0}$ progression observed for **1a** (469 nm), indicating an additional ^{3}MLCT/^{3}LC-based minor contribution to the observed emission for this complex. Small sharp features can also be observed superimposed on the emission band for **3a** at 77 K whose position is invariant with excitation wavelength and are also tentatively assigned to vibronic progressions of the ^{3}MLCT/^{3}LC state. It should be noted that similar sharply resolved ^{3}MLCT/^{3}LC state progressions are observed in the 77 K emission spectrum of the related complex $[Ir(ptz^{Ad})(ptz^{Me})(pytz^{Ad})]^+$ (where $ptz^{Ad}H$ and $ptz^{Me}H$ = 1-adamantyl- and 1-methyl-4-phenyl-1,2,3-triazole respectively and $pytz^{Ad}$ = 1-adamantyl-4-(pyrid-2-yl)-1,2,3-triazole) and the fluorinated analogue $[Ir(dfptz)_2(pytz)]^+$ (dfptz = 4-(2,4-difluorophenyl)-1,2,3-triazole)) rather than broad ^{3}MLCT/^{3}LL′CT emission as previously reported by De Cola and co-workers.[32,33] Thus, at low temperature **1c** and **3a** show dual-emission behavior.

Several examples of dual emissive iridium(III) complexes are known,[35−43] e.g. molecular dyad complexes appended with fluorophores in which the two chromophores are electronically insulated from each other and thus act with photophysical independence. There are also some rare examples of dual phosphorescent complexes in which emission stems from two triplet states, a ^{3}MLCT-based state and a purely ligand-centered (^{3}LC) state, which are of approximately the same energy but are highly distinguishable in terms of band shape and sensitivity to solvent polarity.[36,37,40]

Since the emission spectra of complexes **1b**, **1c**, and **2c** include some significant changes and switching of the emitting state between rigid matrix and fluid medium, we recorded temperature-dependent emission spectra from 100 to 200 K for complexes **1a**−**2c** (Figure 7). Variable temperature emission spectra obtained for **1a**, **2a**, and **2b** are observed to diminish in intensity upon warming from 100 K, with spectral broadening but retention of vibronic progressions in each case without any significant shift in the wavelength of observed maxima.

For **2c**, warming from 100 to 110 K results in a reduction in emission intensity of the ^{3}MLCT/^{3}LC-based progressions at higher energy and the growth of a broad feature between 570 to 700 nm assigned to luminescence from the ^{3}MLCT/^{3}LL′CT state. At 120 K the ^{3}MLCT/^{3}LL′CT-based band dominates the spectrum, with ^{3}MLCT/^{3}LC-derived features having almost disappeared. At 130 K and above, the switching of emitting state is complete and only ancillary ligand-based ^{3}MLCT/^{3}LL′CT state emission is observed.

Between 100 and 200 K the emission band of **1c** is observed to reduce in intensity and the maximum to red-shift by approximately 70 nm with a concomitant reduction in intensity of the weaker sharp ^{3}MLCT/^{3}LC-based emission at 467 nm. The red-shift in the dominant emission band upon reaching 110 K reveals a second weak emission feature at around 500 nm, which is tentatively assigned to the $\nu_{0\rightarrow1}$ progression from ^{3}MLCT/^{3}LC-based emission. Similarly to **2c** these ^{3}MLCT/^{3}LC-based features disappear by 130 K as the glass transitions to fluid.

Upon warming, the vibronic progressions in the variable-temperature emission spectra for **1b** diminish in intensity and broaden between 100 and 120 K (Figure 7). Between 110 and 125 K emission is observed to increase in intensity at wavelengths longer than 560 nm as ^{3}MLCT/^{3}LL′CT-based emission becomes the dominant feature. However, unlike the variable-temperature emission spectra of **2c**, the ^{3}MLCT/^{3}LL′CT-based vibronic progressions are observed to persist for **1b** throughout the temperature regime studied and up to room temperature. These features are even retained in emission spectra for solutions heated to 330 K, suggesting that, above the glass transition temperature, the ^{3}MLCT/^{3}LC and ^{3}MLCT/^{3}LL′CT states in **1b** are both populated and potentially in equilibrium, resulting in the dual emission behavior that is preserved at and above room temperature.

Photoluminescence lifetime data was collected by time-correlated single photon counting (Table 2). No clear trends can be discerned across the series as might have been expected from energy-gap law considerations. This may stem from the interplay and involvement of emitting states of different character. For the higher energy emitters it is also possible that triplet metal-centered state mediated quenching may also play a role.[44] We therefore prefer not to offer deeper interpretations of this data (however, it is interesting to note that the radiative decay rate constants, k_r, for those complexes exhibiting ^{3}MLCT/^{3}LL′CT-based emission are higher ($2.25-3.33 \times 10^{-5}$ s^{-1} in aerated acetonitrile) than the corresponding rate constants for the ^{3}MLCT/^{3}LC emitters ($0.84-1.55 \times 10^{-5}$ s^{-1})). Interestingly, however, emission lifetime data collected at several wavelengths across the spectrum for the dual-emissive complex **1b** fit to a single exponential decay despite emission deriving from two states (Table 2 and Figure S28). Addition of a second exponent leads to no significant improvement to the fitting of the data. It may be that lifetimes for the ^{3}MLCT/^{3}LC and ^{3}MLCT/^{3}LL′CT states in **1b** are very similar to one another such that they cannot be differentiated,[45] or that being in equilibrium on a time scale far shorter than radiative lifetimes they therefore act as a single emitting state. Lifetime data for **2b** (in degassed acetonitrile) and **2c** (in aerated acetonitrile) give rise to biexponential decay. For **2b** it is possible that this arises due to two distinct ^{3}MLCT/^{3}LC states given the asymmetry of the pymtz ligand, which will make the two dfppy ligands inequivalent. Biexponential decay for **2c** is unexpected but may derive from differing favorable conformations of the pyztz benzyl substituent. Lifetime data recorded in 2-methyltetrahydrofuran during collection of temperature dependent emission spectra are however monoexponential (Table S1).

To summarize, the steady-state luminescence data has highlighted three different behaviors: (i) single emitters that are insensitive to rigid matrix effects and temperature, in terms of the nature of the emissive state (**1a**, **2a**, **2b**, **3a**−**3c**); (ii) one single emitter that switches from one emissive state at 77 K to another emissive state at room temperature (**2c**); (iii) a dual

https://dx.doi.org/10.1021/acs.inorgchem.9b03003
Inorg. Chem. XXXX, XXX, XXX−XXX

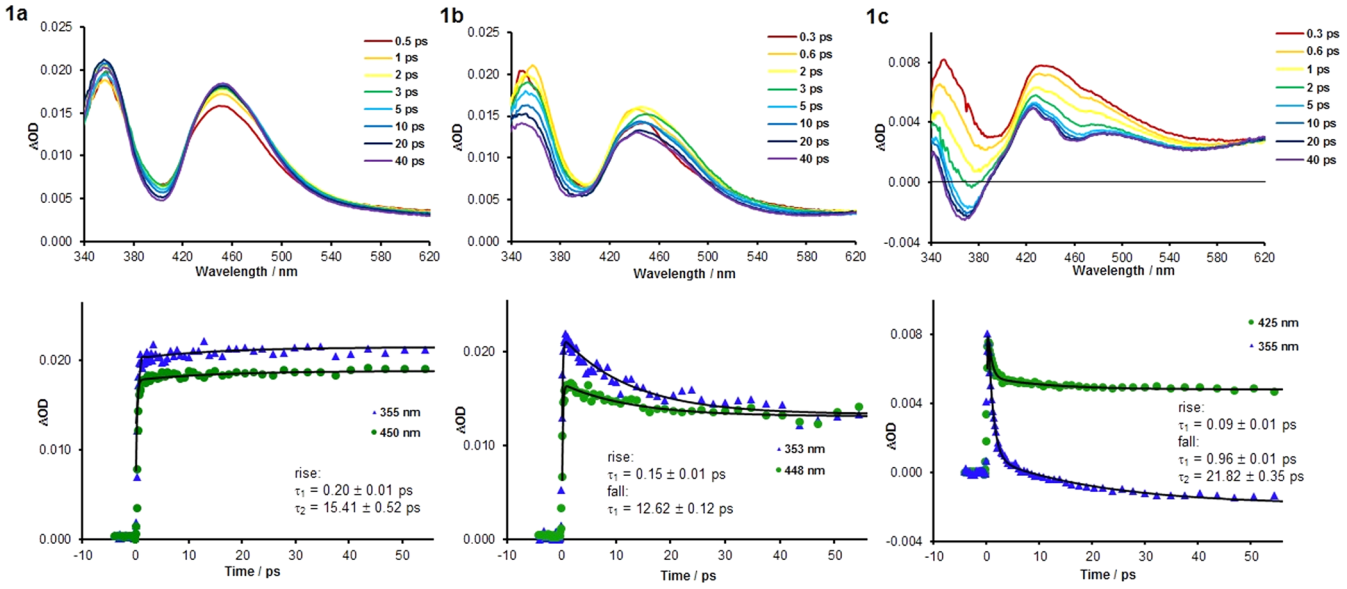

Figure 8. UV−visible transient absorption spectra for complexes **1a−c** in acetonitrile solutions at room temperature (top, λ_{ex} = 285 nm) and associated time profiles with kinetic fits from global analysis (bottom).

emitter over a broad temperature and solvent range (**1b**), a case that has been scarcely described.

Transient Absorption Studies. Given the highly intriguing nature of our steady state emission data reported above, we felt compelled to carry out fs-ps transient absorption spectroscopic experiments on complexes **1a** to **2c** in order to capture the time evolution of anticipated energy transfer processes for **1b**, **1c** and **2c**, whose emissive excited-state character changes between rigid glasses and fluid solutions. Indeed, recently the groups of Elias[46] and Kang[47] and their respective co-workers have utilized transient absorption spectroscopy to study the excited-state energy transfer processes for $[Ir(C^N)_2(N^N)]^+$-type complexes. The complex $[Ir(dfppy)_2(pic)]$ (pic = 2-picolinate) exhibits structured ^{3}MLCT/^{3}LC-based emission bands at both room temperature and 77 K. On the other hand, the complexes $[Ir(dfppy)_2(N^N)]^+$, where N^N is bpy and 1,10-phenanthroline, exhibit broad featureless emission bands arising from ^{3}MLCT/^{3}LL′CT states in fluid solutions at room temperature. They have observed structured emission bands arising from ^{3}MLCT/^{3}LC states at 77 K in frozen solution glass matrices. Transient absorption spectra for $[Ir(dfppy)_2(pic)]$ reveal bands assigned to the photoexcited ^{3}MLCT/^{3}LC states which have effectively infinite lifetime on the time scale of the transient experiment. For the cationic complexes early transients formed immediately after photoexcitation are observed to undergo changes with decay lifetimes of between 2 and 4 ps assigned to an energy transfer process from initially populated ^{3}MLCT/^{3}LC states to the ^{3}MLCT/^{3}LL′CT states responsible for steady state emission in each case.

Transient absorption spectra and associated time profiles for **1a** to **1c** are displayed in Figure 8 with comparable data for the fluorinated complexes **2a** to **2c** given in the Supporting Information (Figure S29).

Transient spectra for **1a** are characterized by two absorption maxima appearing at 355 and 460 nm, assigned to absorption from the ^{3}MLCT/^{3}LC state, separated by what appears to be a ground-state bleach feature at 400 nm superimposed upon the positive transient absorption profile. These features closely match those observed previously in nanosecond time-resolved data for similar complexes reported by De Cola and co-workers.[48] Similar spectra are observed for **2a** and **2b** (Figure S29), however the transient maxima are blue-shifted relative to those of **1a** such that the higher energy and more intense band is shifted outside of the available spectroscopic window, and the bleach feature, positioned between 340 and 380 nm, is less intense. Analysis of the transient spectra for **1a**, **2a** and **2b** reveals time profiles reminiscent of those for the ^{3}MLCT/^{3}LC emitter $[Ir(dfppy)_2(pic)]$ with very little change in spectral intensities and band shapes over the time scale studied (3 ns).[47] Global analysis fitting reveals, however, that in addition to the rapid rise time (~0.2 ps) for these three complexes there is a second subtle but discernible process with a longer rise time of between 5 and 15 ps (Table S2). Given the asymmetry of the complexes due to the N^N ligands, this is tentatively assigned to equilibration between different available ^{3}MLCT/^{3}LC states involving the two inequivalent C^N ligands.

In line with the fundamentally different steady state emission behavior of **1c** and **2c** relative to **1a**, **2a** and **2b**, the evolution of transient spectra for these pyrazine-based complexes also show stark differences. Initial transients that appear in the first picosecond closely resemble those discussed above, supporting the notion that **1c** and **2c** are initially excited to ^{3}MLCT/^{3}LC states. However, rapid evolution fitted to a biexponential decay is observed with two time constants of 0.9−2.8 and 21.8−24.6 ps. During this evolution the ^{3}MLCT/^{3}LC-based transient absorption features are observed to blue-shift and reduce in intensity. As the lower energy absorption features at wavelengths beyond 420 nm diminish, more structured absorptions are observed with a sharp structured feature at around 425 nm for **1c** along with a broad absorption band at 490 nm. The higher energy transient band at 350 nm is observed to decay to a greater extent while the bleach becomes more prominent such that it becomes a genuinely negative feature after 5 to 10 ps. Spectral features in transient absorption spectra after this time are therefore assigned to the ^{3}MLCT/^{3}LL′CT states of **1c** and **2c**. Thus, it can be seen from this data that clearly and

https://dx.doi.org/10.1021/acs.inorgchem.9b03003
Inorg. Chem. XXXX, XXX, XXX−XXX

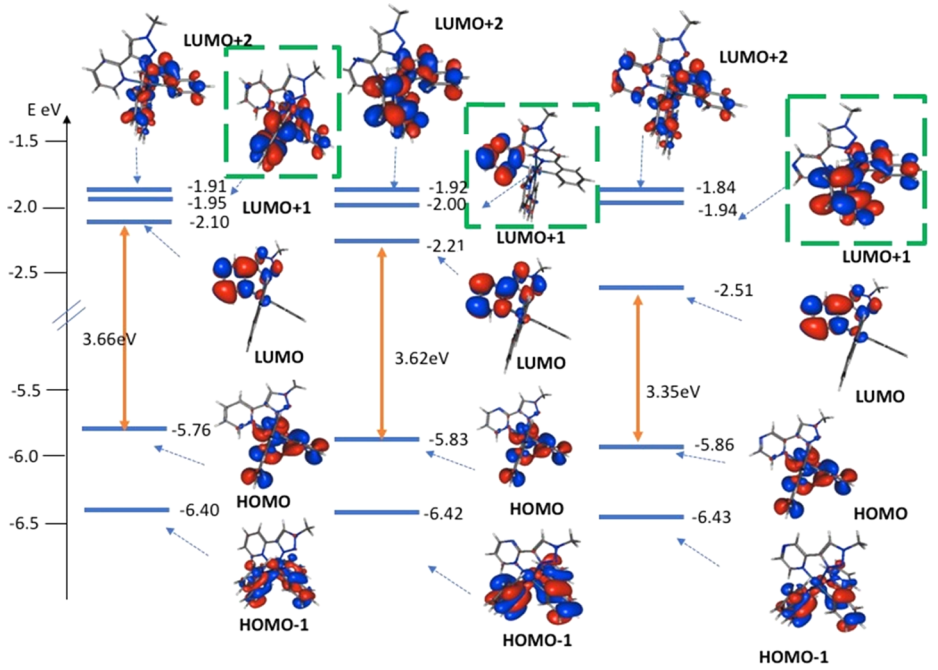

Figure 9. Molecular orbital energies and isosurface plots for HOMO−1 to LUMO+2 for complexes **1a** (left), **1b** (middle), and **1c** (right). The green squares highlight LUMO+1, whose localization varies.

conveniently distinguishable transient absorption profiles are discernible for ^{3}MLCT/^{3}LC and ^{3}MLCT/^{3}LL′CT states. Due to the asymmetry of the complexes the two time constants may reflect the decay to the ^{3}MLCT/^{3}LL′CT state from two distinct ^{3}MLCT/^{3}LC states characterized by which of the C^N ligands the excited electron resides. On the other hand the longer decay process may also be contributed to by vibrational cooling and energy redistribution in the ^{3}MLCT/^{3}LL′CT state.

In line with its peculiar steady state spectroscopic behavior, **1b** is again unique among the complexes studied. Initial transient spectra at 1 ps after excitation closely resemble those of the other five complexes, confirming that a ^{3}MLCT/^{3}LC state is initially populated. The spectra are subsequently observed to undergo rapid evolution with a time constant of 12.6 ps. This involves a blue-shift and drop in intensity of the absorption feature at around 450 nm. A larger fall in intensity is observed for the higher energy absorption feature at 350 nm while the bleach feature at around 400 nm undergoes a small blue shift and becomes less positive in magnitude. These spectral changes are less dramatic than those observed for **1c** and **2c**, and overall the transient spectra sit somewhere between those for **1a** and **1c**. Whereas the transient data for **1c** and **2c** suggest complete depopulation of the ^{3}MLCT/^{3}LC state to yield the ^{3}MLCT/^{3}LL′CT state, the data for **1b** is consistent with the partial transfer of population to the ^{3}MLCT/^{3}LL′CT state and equilibration with the initially populated ^{3}MLCT/^{3}LC state, in agreement with the dual-emissive character suggested from steady state emission spectra.

Transient absorption data are therefore in perfect agreement with our steady state spectroscopic data and time-resolved studies on related systems reported elsewhere by others. At this stage, a detailed theoretical study is vital in order to fully rationalize the photophysical peculiarities for the series of complexes reported.

Ground-State Molecular Orbitals. In order to gain a deeper understanding of the photophysical properties of the complexes described we carried out density functional theory (DFT) calculations. The ground-state geometries of all complexes were optimized substituting the benzyl substituent of the triazole ring with methyl. As the benzyl substituent is expected to have minimal impact on the photophysical properties its simplification then enables reduced computational cost. Figures 9 and S30 and S31 depict the calculated energies of the frontier molecular orbitals for all complexes with accompanying depictions of the corresponding isosurfaces for these orbitals. In each case the highest-occupied molecular orbital (HOMO) is composed of an Ir-based d-orbital in a π-antibonding combination with the π-system of the arene rings of the cyclometalated ligands. The energies of the HOMOs are calculated to undergo stabilization in the order pytz > pymtz > pyztz (**a** > **b** > **c**), presumably due to reduced electron density at the metal as the N^N ligand becomes more electron withdrawing, in broad agreement with electrochemical data. Also in agreement with this data the HOMOs of the dfppy complexes **2a**−**c** are significantly stabilized with respect to those of their ppy and ptz analogues **1a**−**c** and **3a**−**c** respectively.

For all complexes the LUMO is calculated to have N^N π*-character with localization over both the 6-membered azole and triazole rings but with a greater contribution from the former. For each series the energies of the LUMO decrease in the order pytz > pymtz > pyztz (**a** > **b** > **c**), in agreement with electrochemical reduction potentials. In each series the LUMO is stabilized to a greater extent than the HOMO. This leads to a largest HOMO−LUMO gap for the pytz complexes **a** (3.66 to 3.95 eV) and the smallest for the pyztz complexes **c** (3.35 to 3.51 eV), in agreement with the former having the most blue-shifted absorption and emission spectra while those of the latter are the most red-shifted. Across the three series the localization of the LUMO+1 orbital (highlighted by the green boxes in Figures 9, S30, and S31) varies; for **3a**−**c** LUMO+1 is

https://dx.doi.org/10.1021/acs.inorgchem.9b03003
Inorg. Chem. XXXX, XXX, XXX−XXX

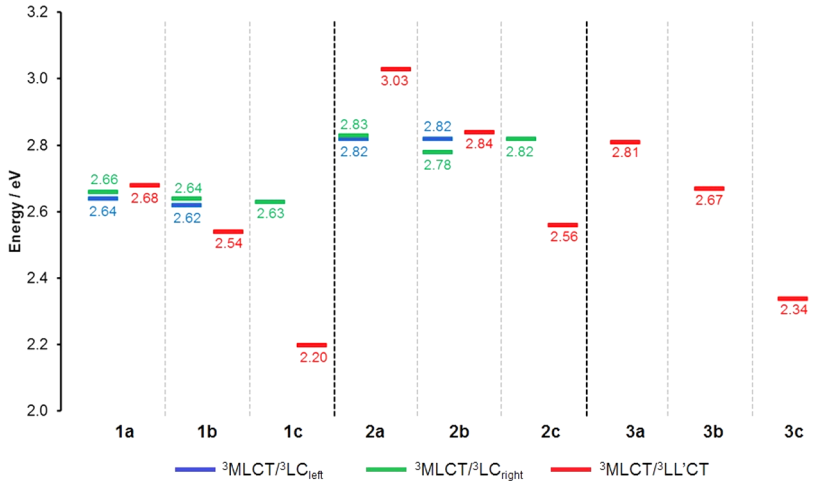

Figure 10. Calculated triplet-state energies for complexes **1a−c**, **2a−c**, and **3a−c** in MeCN using SMD model. Energies are quoted relative to the optimized ground state for each complex, E_{GS} = 0.0 eV.

localized on the ancillary N^N ligand as is LUMO+1 for the pyrimidine complexes **1b** and **2b**. The LUMO+1 orbitals for **1a**, **2a**, **1c** and **2c** are, on the other hand, C^N π^* in character, as are the LUMO+2 orbitals for all the ppy and dfppy complexes (which in some cases are mixed with N^N π^*-character). For **3a−c** the lowest ptz-localized C^N virtual orbital is LUMO+2, which appears to be significantly destabilized relative to the corresponding lowest ppy and dfppy based C^N π^* orbitals of **1a−c** and **2a−c**. This is indicative of the reduced electron-accepting ability of phenyltriazole vs phenylpyridine, which is exploited in this work to tune the gap between ^{3}MLCT/^{3}LC and ^{3}MLCT/^{3}LL′CT excited states.

The experimental photoluminescence studies have evidenced three types of emitter (^{3}MLCT/^{3}LC only, ^{3}MLCT/^{3}LL′CT only, or dual emission from both). We will now try to find some theoretical support for this behavior, starting from the ground-state molecular orbital diagrams. The LUMO for all complexes is of N^N π^* character, yet not all emission spectra are broad and featureless, as one would expect for ^{3}MLCT/^{3}LL′CT-based emission. Thus, the ordering of the emissive excited states does not follow the ordering of the ground-state unoccupied orbitals whose population with which these states would be expected to be associated. Therefore, it is necessary to extend our reasoning beyond a simple consideration of the LUMO except, perhaps, in cases where it is well-below all other vacant orbitals. This would be the case for phenyltriazole family **3**, which exhibits an N^N-based LUMO, well-separated from the C^N-based vacant orbitals, a specificity that again fits with the observed ancillary-based emission at all temperatures. **1a** and **2a** display closer-lying N^N and C^N vacant orbitals, which means that one could expect the two types of excited state to be close in energy. Solely C^N-based emission is observed, however, which highlights the great importance of the LUMO+1 for these complexes. Both the localization of the LUMO+1 and the energy gap between the N^N and C^N vacant orbitals are crucial. Unlike **1a** and **2a**, **1b**, and **2b** display an N^N-based LUMO+1. Therefore, one might expect the ancillary ligand-based excited states to be lower in energy in the **b** series than in the **a** series, and if close enough in energy to the corresponding C^N ligand-based ^{3}MLCT/^{3}LC state, then complexes in the **b** series could be dual emitters. While comparative analysis of the ground-state molecular orbitals provides useful insights, these data alone are insufficient to fully rationalize the peculiar emission behavior observed across the complexes reported. It is therefore vital to additionally consider the optimized triplet excited states that give rise to emission.

Lowest Triplet States. To better understand the emission properties of the complexes, minima for the lowest lying triplet states were optimized. The deliberate differentiation of the two C^N ligands by using an asymmetric ancillary ligand can give rise to two distinct ^{3}MLCT/^{3}LC states.[49] For **1a**, **1b**, **2a**, and **2b** two ^{3}MLCT/^{3}LC minima, ^{3}MLCT/^{3}LC$_{left}$ and ^{3}MLCT/^{3}LC$_{right}$, were optimized on the lowest energy triplet potential energy surface (T_1 PES) (the energies of the lowest triplet excited states for all complexes quoted relative to their respective optimized ground-state energies are depicted in Figure 10). Plots of the spin densities for these states are provided in Figure S32. For the states labeled with the subscript "left", the spin density is distributed over the metal center and the C^N ligand situated trans to the triazole ring of the ancillary ligand, whereas those labeled "right" involve the C^N ligand trans to the ancillary ligand 6-membered ring. While there have been several elegant computational studies of the ^{3}PES of phosphorescent iridium(III) complexes, these have focused on ^{3}MLCT state deactivation by triplet metal-centered (^{3}MC) states[50−57] or the *fac*/*mer*-isomerization resulting from ^{3}MC state population from a ^{3}MLCT state and subsequent geometry evolution.[58] To the best of our knowledge, this is the first time that multiple ^{3}MLCT-based admixed states have been optimized for individual complexes.

For complexes **1c** and **2c**, ^{3}MLCT/^{3}LC$_{left}$ states could not be located on the T_1 PES, suggesting that this state is not a minimum, is a very shallow one, or is a higher lying triplet state. For complexes **3a−c**, only a ^{3}MLCT/^{3}LL′CT state could be located on the T_1 PES. This type of excited state is found in all complexes. For each series **1**, **2**, and **3**, the ^{3}MLCT/^{3}LL′CT state is observed to be highest in energy for pytz complex **a** and lowest in energy for pyztz complex **c**, in agreement with spectroscopic data. The lowest excited triplet state does not always result from HOMO−LUMO excitation, thus a straightforward transposition of the electrochemical data to the excited states is not always correct.

https://dx.doi.org/10.1021/acs.inorgchem.9b03003
Inorg. Chem. XXXX, XXX, XXX−XXX

For **1a**, **2a**, and **2b**, which exhibit structured emission bands indicative of a luminescent state of ^{3}MLCT/^{3}LC character, calculations confirm that these states are lower in energy than their respective ^{3}MLCT/^{3}LL′CT states. Thus, ^{3}LC-admixed states would be expected to dominate the emission properties for these complexes, in agreement with a classical Kasha behavior. Such ^{3}MLCT/^{3}LC states do not derive from a HOMO−LUMO excitation. The "left" and "right" ^{3}LC-admixed states for these complexes are calculated to be very close in energy to each other, thus their individual emissions are probably indistinguishable, both in terms of energy and luminescence lifetime.[59]

For **1c** and **2c**, the ^{3}MLCT/^{3}LL′CT state, which does arise from HOMO−LUMO excitation, is calculated to be significantly lower in energy than the ^{3}MLCT/^{3}LC$_{right}$ state by 0.43 and 0.26 eV respectively, in agreement with the broad featureless emission bands exhibited in their room-temperature solution spectra. This is in line with the previously mentioned large gap between N^N-based LUMO and C^N-based LUMO +1. This is in agreement with experimental data revealing that when initially populated upon photoexcitation the ^{3}MLCT/^{3}LC state will be rapidly depopulated to the ^{3}MLCT/^{3}LL′CT state from which emission then occurs. The ^{3}MLCT/^{3}LC states of **2a** and **2b** are stabilized relative to the ^{3}MLCT/^{3}LL′CT states for this series in comparison to the relative energies of the same states for **1a−c**. This stems from the electron-withdrawing fluorine atoms of the dfppy ligands which leads to stabilization of the vacant orbitals on these ligands and thus a greater perturbation of the ^{3}MLCT/^{3}LC states relative to the ^{3}MLCT/^{3}LL′CT states, thereby bestowing a larger energy gap between these states for **1c** compared to those for **2c**. For **3a−c**, for which ^{3}MLCT/^{3}LC minima could not be located on the T_1 PES (high-lying C^N-based vacant orbitals), the data are consistent with the interpretation of the broad featureless emission bands observed both in fluid solution and in a frozen medium at low temperature as arising from ^{3}MLCT/^{3}LL′CT states.

For **1b**, which displayed the smallest gap between N^N and C^N vacant orbitals (Figure 9) and thus could be expected to be a good candidate for dual emission, the ^{3}MLCT/^{3}LC$_{left}$ and ^{3}MLCT/^{3}LL′CT states are calculated to be separated by only 0.08 eV. This contrasts with the 0.35 eV energy difference based on the wavelengths of the emission maxima derived from ^{3}MLCT/^{3}LC (474 nm, Table 1) and ^{3}MLCT/^{3}LL′CT (547 nm). The actual difference in energy between emission bands for these two states stems from the vibronic contributions involved in the electronic transition. Indeed for the ^{3}LC case, the highest energy transition in the spectra corresponds to the 0−0 transition (474 nm), while for the ^{3}LL′CT case the emission maxima (547 nm) coincides with the 0−1 transition (*vide infra*), leading in this latter case to a maximum emission wavelength red-shifted by 60 nm (0.3 eV), a value that is reproduced on both computed and experimental spectra displayed in Figure 11. A deeper analysis of the vibronic progressions observed in emission spectra is presented in the next section. As the emission spectrum of **1b** appears to have overlapping contributions from both structured ^{3}MLCT/^{3}LC-based and unstructured ^{3}MLCT/^{3}LL′CT-based bands which maintain their relative intensities upon heating to approximately 330 K, the calculated data therefore support the experimental interpretation that these states are essentially isoenergetic and that **1b** is a dual emitter over a broad range of temperatures.

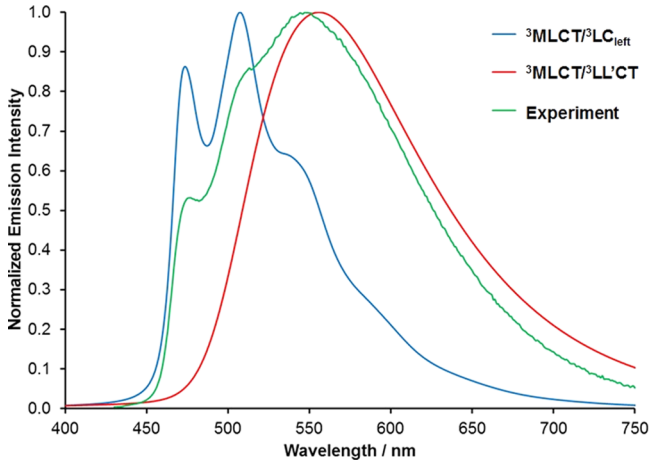

Figure 11. Comparison of calculated VRES for **1b** at 300 K from the ^{3}MLCT/^{3}LC$_{left}$ and ^{3}MLCT/^{3}LL′CT states (ethanol, SMD) with the experimentally observed emission spectrum in room-temperature acetonitrile solution.

Vibrationally Resolved Emission Spectra (VRES). VRES calculated for all complexes at 300 and 77 K reproduce the fine structure of the experimentally acquired spectra and help to confirm the assigned emitting excited-state character. Spectra for **3a−c** at 300 K are in good agreement with experimentally obtained spectra and are characterized by broad featureless bands that red-shift in the order **3a** < **3b** < **3c** (VRES spectra for all complexes are provided in Figure S35). Spectra calculated for the ^{3}MLCT/^{3}LC$_{right}$ states of **2a** and **2b** are near coincident and display vibronic fine structure in agreement with both experimental data and the assignment of the nature of the emitting excited state, while the calculated spectrum for the ^{3}MLCT/^{3}LL′CT state of **2c** appears as an expected broad featureless band. Spectra for emission from the ^{3}MLCT/^{3}LC state for **1a**, **1b**, and **2a−c** calculated at 77 K reproduce the observed sharp major bands as well as the other fine structural features seen in the experimentally determined emission profiles. For **1c**, the calculated ^{3}MLCT/^{3}LL′CT-based emission spectra at both 77 and 300 K match the broad featureless bands observed experimentally. The calculated 300 K emission spectra for **1a** and **1b** deriving from their ^{3}MLCT/^{3}LC states match the experimentally observed vibronic structuring. To provide a better understanding of the emission band shape of this family of compounds, we sought to identify the vibrations responsible for the origin of this multipeak emission spectrum by following the protocol described in Figures S36−S40. Our analysis shows that ^{3}MLCT/^{3}LC emission spectra can be viewed as several superimposed progressions of different bandshapes. Contributions are due to mixed excitation of several effective vibrational modes (C−C and C−N stretching, C−H wagging, and valence deformation such as CCH, CCC, and CCN of phenylpyridine and ancillary ligand) and are spread over the three bidentate ligands. Concerning ^{3}MLCT/^{3}LL′CT emission, our analysis as detailed in Figures S36−S40 allowed us to identify the apparent emission maximum mainly as the $v_{0\rightarrow1}$ vibronic contribution corresponding to an effective mode involving in-plane C−$H_{aromatic}$ wagging and C−C stretching localized solely on the ancillary ligand.

https://dx.doi.org/10.1021/acs.inorgchem.9b03003
Inorg. Chem. XXXX, XXX, XXX−XXX

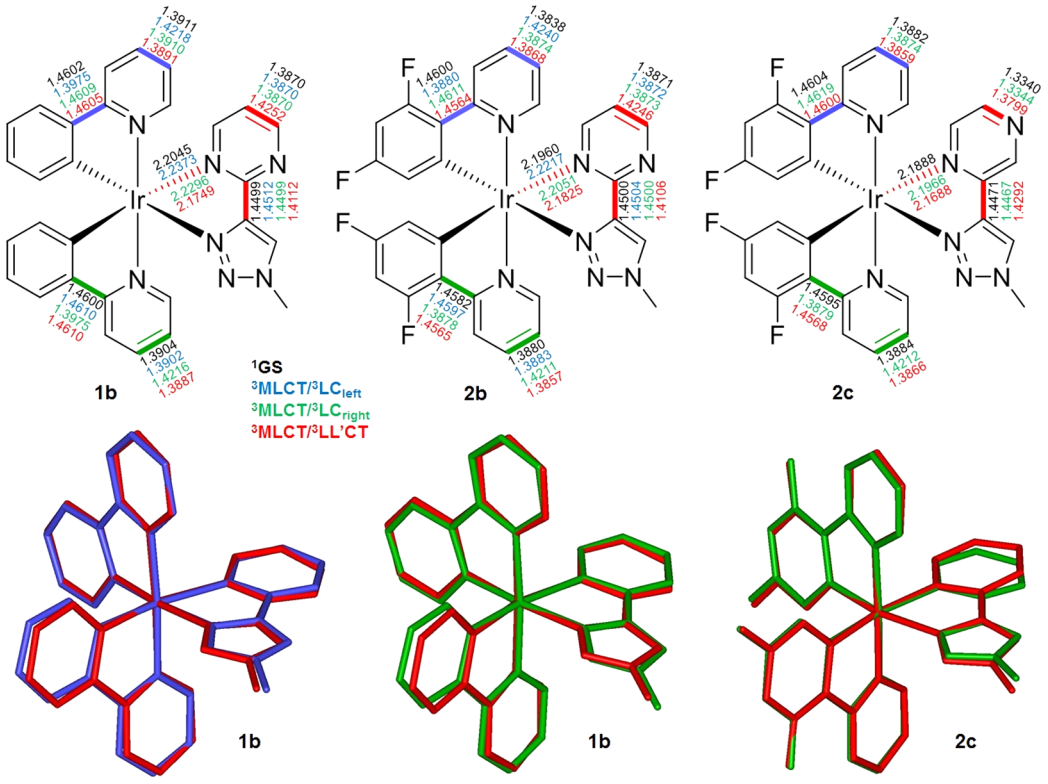

Figure 12. Top: Summary of lengths (Å) of key selected bonds (highlighted in bold) for the ^{1}GS (black numbers), ^{3}MLCT/^{3}LC$_{left}$ (blue numbers), ^{3}MLCT/^{3}LC$_{right}$ (green numbers), and ^{3}MLCT/^{3}LL′CT (red numbers) states of **1b**, **2b**, and **2c**. Bottom: Overlay of equilibrium geometries for ^{3}MLCT/^{3}LL′CT (red), ^{3}MLCT/^{3}LC$_{left}$ (blue), and ^{3}MLCT/^{3}LC$_{right}$ (green) states of **1b** and **2c**.

For **1b**, the calculated emission spectrum for the ^{3}MLCT/^{3}LL′CT state (red trace on Figure 11) appears as a broader, less structured band red-shifted relative to the calculated ^{3}MLCT/^{3}LC emission band (blue trace on Figure 11). An overlay of these two bands matches well with the experimentally observed emission profile (green trace on Figure 11) with extremely good agreement over the position of emission maxima. This thereby provides further corroboration of the assignment of dual emission from both ^{3}MLCT/^{3}LL′CT and ^{3}MLCT/^{3}LC states of near equal energy.

Matrix Effects. As shown in Figure 10, the energy gaps between the different triplet states are particularly small for **1a** and **2b**. Despite this quasi-degeneracy, the energy and fine structure of the emission bands unambiguously indicate a pure C^N-based emission, instead of dual emission. This is confirmed by theory, which also rules out emission from the ancillary-based triplet state. At this stage, one can propose either that the N^N-based triplet state is not populated or that it has other modes of deactivation. Low-temperature spectroscopic data should bring further insights into this discussion.

The large energy splitting between the two triplet states of complex **2c** would, at first sight, orient the system toward systematic N^N-based emission. However, at 77 K in the frozen matrix, C^N-based emission is observed instead. This initially puzzling result is moderated by the variable-temperature luminescence data (Figure 7), where emission from the ancillary ligand-based state appears as soon as 100−110 K. The first hypothesis that can be put forward invokes matrix effects on the relative energies of the triplet states and thus also on the barrier for their conversion. According to Meyer,[60] with the solvent being frozen to accommodate the complex in its ground state, excited states with a dipole moment similar to the ground state will be stabilized to a greater degree in the frozen matrix than excited states with a significantly different dipole moment. For the ground and ^{3}LC-admixed states, the dipole moment bisects the rings of the ancillary ligand for **1a** and has a similar magnitude (15.1−15.5 D) but in the ^{3}LL′CT state is nearly orthogonal in direction compared to the ground state and is smaller in magnitude (4.73 D, Figure S41). Therefore, one expects the ^{3}MLCT/^{3}LL′CT state to be significantly destabilized with respect to the ^{3}MLCT/^{3}LC state in frozen matrices, possibly leading to state reordering. As a result, no emission is observed from the N^N-based state for **2c** at 77 K. As soon as the matrix becomes more fluid, the N^N-based state starts to contribute to the experimental emission spectrum from 110 K (dual emission), and a pure N^N-based emission is observed at and above 120 K (Figure 7). For **1c**, the larger energy spacing between the ^{3}MLCT/^{3}LL′CT and ^{3}MLCT/^{3}LC states compared to that in **2c** results in the retention of ^{3}MLCT/^{3}LL′CT-based emission as the dominant feature at 77 K. However, the two states are evidently brought into much closer proximity in the glass matrix, as revealed by the appearance of weaker vibronic progressions and dual-emission in the low-temperature spectra (*vide supra*).

Triplet−Triplet Interconversion Pathways. Despite the fact that rigidity effects are not included in our calculations, purely thermodynamic considerations (energy gaps between triplet states) are not sufficient to rationalize the totality of the photoluminescence data. We therefore also envisaged kinetic considerations through the calculation of energy paths for triplet−triplet state interconversions, in order to obtain the corresponding energy barriers. First, we start by describing the structural changes between the various triplet states.

https://dx.doi.org/10.1021/acs.inorgchem.9b03003
Inorg. Chem. XXXX, XXX, XXX−XXX

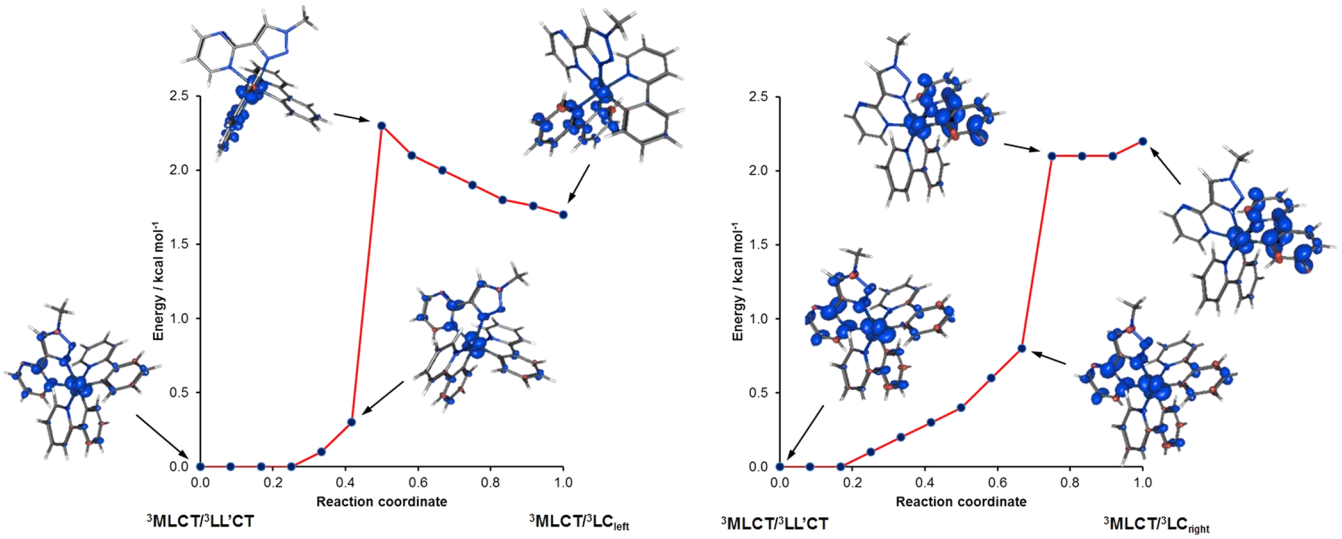

Figure 13. Spin density plots and T_1 PES minimum energy path between the ^{3}MLCT/^{3}LL′CT state and ^{3}MLCT/^{3}LC$_{left}$ (left panel) and ^{3}MLCT/^{3}LC$_{right}$ (right panel) states for **1b** from a nudged elastic band optimization calculation (MeCN using SMD model).

Upon examination of the major changes to bond lengths between the optimized geometries of the ground states, left and right ^{3}MLCT/^{3}LC states, and the ^{3}MLCT/^{3}LL′CT state, a clear common picture emerges for the ligand hosting the electron density in the excited state; this involves a shortening of the intercyclic bond and lengthening of the $\beta-\gamma$ bond in the most π-accepting ring, i.e., py in ppy and dfppy, and the 6-membered ring in the ancillary ligand (see bonds highlighted in bold in Figure 12). For the ^{3}MLCT/^{3}LC states, the intercyclic C−C bond is observed to shorten by ∼0.06 Å (compared to the ground state) for the C^N ligand on which the state is localized (as observed in the localized ^{3}MLCT state of $[Ru(bpy)_3]^{2+}$).[61] This is accompanied by an elongation of the C−C bond at the $\beta-\gamma$ bond of the pyridine ring (also highlighted bold in Figure 12). The Ir−N bond to the 6-membered heterocycle of the N^N ligand is observed to elongate compared to the ground state. In the ^{3}MLCT/^{3}LL′CT state, these C^N bonds return to their approximate ground-state values. The intercyclic C−C bond of the ancillary ligand (receiving the electron density) is observed to shorten compared to those in the ground and ^{3}MLCT/^{3}LC states, while the $\beta-\gamma$ C−C/N bond of the 6-membered ring elongates. This is accompanied by a shortening of the Ir−N bond to the pyridine/pyrimidine/pyrazine ring compared to both the ground and ^{3}LC-admixed states.

Figure 12 (bottom) displays overlaid geometries for **1b** and **2c**. These reveal large structural differences between the ^{3}LC- and ^{3}LL′CT-admixed states for these complexes. For example, the plane of the pyrazine ring in **2c** is significantly inclined with respect to the N−Ir−N plane in the ^{3}MLCT/^{3}LL′CT state, resulting in a change in the position of the atoms for this ring compared to the ^{3}MLCT/^{3}LC$_{right}$ state. At 77 K, the rigid glass matrix impedes these atomic motions and leads to destabilization of the ^{3}LL′CT-admixed state. In combination with the likely larger effect due to the change in the dipole moment with respect to that of the ground state (*vide supra*), this traps **1b** and **2c** in the ^{3}MLCT/^{3}LC state giving rise to structured emission profiles comparable to those observed for the corresponding complexes **1a**, **2a**, and **2b**. Above the glass transition temperature, these intramolecular and solvent motions are enabled, leading to ^{3}MLCT/^{3}LL′CT state emission for **2c** and to dual emission for **1b**.

Nudged elastic band (NEB) calculations[62,63] have recently emerged as a powerful tool for exploring the minimum energy path between excited-state minima, thus characterizing excited-state PES topologies of photoactive metal complexes.[64,65] We therefore carried out NEB minimum energy path (MEP) calculations between both the ^{3}MLCT/^{3}LC state minima and ^{3}MLCT/^{3}LL′CT state minimum of **1b** (Figure 13), between the ^{3}MLCT/^{3}LC$_{left}$ and ^{3}MLCT/^{3}LC$_{right}$ state minima for **1b** (Figure S42), and between the ^{3}MLCT/^{3}LC and ^{3}MLCT/^{3}LL′CT state minima for **2c** (Figure S43). Concerning the ^{3}MLCT/^{3}LC$_{left}$−^{3}MLCT/^{3}LC$_{right}$ interconversion, two nearly degenerate states of the same electronic nature, in equilibrium with one another, behave like a single emissive state (as suggested by Tor for heteroleptic Ru(II) complexes).[59] NEB calculations between ^{3}MLCT/^{3}LC$_{left}$ and ^{3}MLCT/^{3}LC$_{right}$ in the case of **1b** (Figure S42) were particularly difficult to converge with oscillations between two electronic states. This could possibly be interpreted as an equilibrium between the two C^N-based states, as illustrated by the presence of both states along the whole MEP and in agreement with transient absorption data.

As can be seen from the MEPs, the conversions between states of different electronic nature (different orbital parentage) take place through a sharp transition with an abrupt change in energy accompanied by a sudden switch in the spin density localization, instead of a gradual mixing of the two states (no transition state with mixed spin density could be captured). Thus, the transitions observed here suggest a crossing point between two weakly coupled excited states and suggests that transition between these states operates via "through-space" rather than "through-bond" coupling. This is reminiscent of the interligand electron hopping characterized by ESR[66] and reproduced in dynamics studies[67] between localized ^{3}MLCT states of $[Ru(bpy)_3]^{2+}$. Returning to this work, even though no transition state (TS) could be analytically captured, the tangent to the PES at the highest energy point is a good estimate of the TS mode of the saddle point. For complexes **1a** and **1b**, visualization of these TS modes (Figure S44) shows a seesaw motion of the C^N ligand

https://dx.doi.org/10.1021/acs.inorgchem.9b03003
Inorg. Chem. XXXX, XXX, XXX−XXX

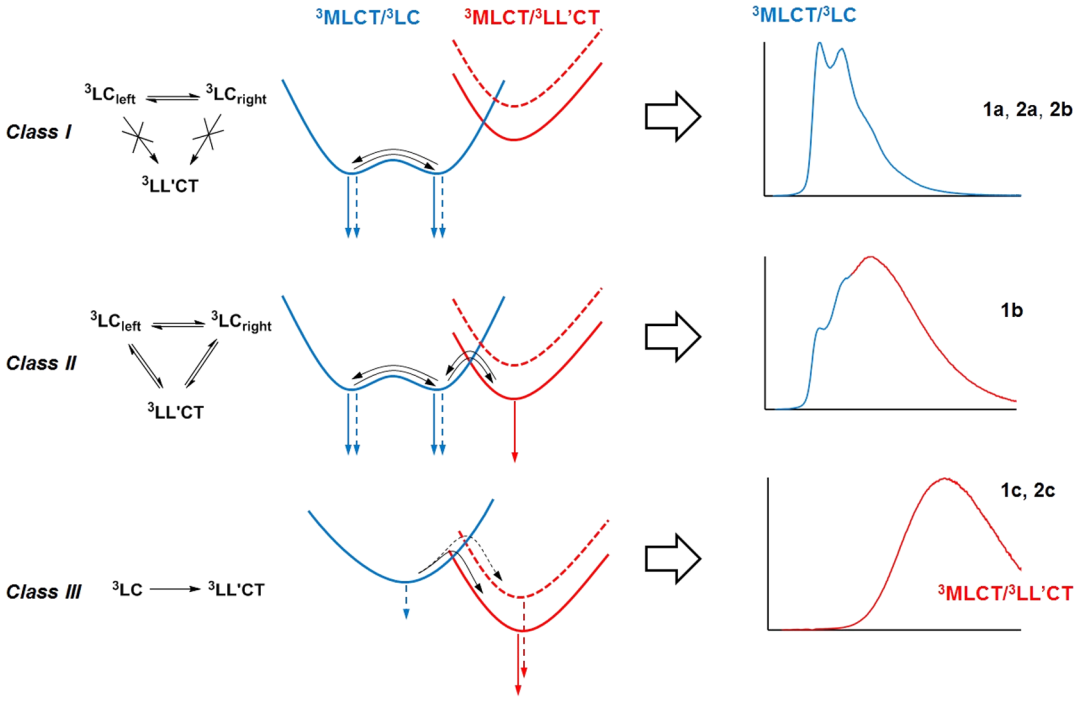

Figure 14. Qualitative potential energy surface diagram describing the excited-state evolution and emission behavior of Class I (**1a**, **2a**, and **2b**), Class II (**1b**), and Class III (**1c** and **2c**) emissive $[Ir(C^N)_2(N^N)]^+$ complexes. Downward arrows represent radiative deactivation pathways. Solid lines and arrows represent processes in fluid solutions; dashed lines and arrows represent process in cryogenic glass matrices at 77 K.

not involved in the electron transfer, in line with the proposed through-space mechanism for the ^{3}MLCT/^{3}LC$_{left}$–^{3}MLCT/^{3}LL′CT population transfer.

The topology of the state crossing exemplified on Figure 13 is particularly unfavorable to conversion by tunnelling effects, given the large difference in the slopes of the two surfaces. Therefore, the conversion may only occur by vibrational coupling. In an attempt to identify key bond vibrations that are involved in the conversion between ^{3}MLCT/^{3}LL′CT and ^{3}MLCT/^{3}LC$_{left}$ states through appropriate promoting modes, calculation of dimensionless displacement of nuclear coordinates (DDNC) was carried out for **1b**. This reveals a number of vibrations that lead to major productive geometrical changes at 963 (Ir–C and Ir–N bonds toward C^N ligand), 989 (Ir–N bonds toward N^N ligand), 1302 (triazole ring and intercyclic bond of the C^N left ligand), and 1399 cm^{-1} (intercyclic bond of the N^N ligand).

We have examined the variation of the bond lengths shown in bold in Figure 12 along the MEP between ^{3}MLCT/^{3}LC$_{left}$ and ^{3}MLCT/^{3}LL′CT states for **1b** (Figure 13). This reveals that the lengths of both the intercyclic C–C bond and the β–γ C–C bond of the pyridine ring of the ppy ligand trans to pyrimidine are largely invariant throughout the MEP, as would be expected given that at no point does it host the excited electron. However, the corresponding bonds for the other ppy ligand trans to triazole (on which the ^{3}MLCT/^{3}LC$_{left}$ state excited electron resides) as well as the highlighted bonds for the ancillary N^N ligand, undergo an abrupt change at the transition (Figure S45). On either side of this abrupt transition, these bond lengths are also largely invariant. In contrast, examination of the Ir–N bond to the pyrimidine ring reveals a continual contraction along the MEP from ^{3}MLCT/^{3}LC$_{left}$ to ^{3}MLCT/^{3}LL′CT. An analysis of the structural changes along the MEP between the ^{3}MLCT/^{3}LC$_{right}$ and ^{3}MLCT/^{3}LL′CT states reveals an almost identical picture with regards Ir–N and N^N-based bond length changes except that the C^N bond length changes occur in the other ppy ligand. The contraction of this Ir–N bond may therefore provide a strong candidate for a convenient reaction coordinate along which ^{3}MLCT/^{3}LC → ^{3}MLCT/^{3}LL′CT state switching may occur.

Origin of Dual Emission and the Mechanism of Excited-State Interconversion. The combined data allow significant insight into the photophysical behavior of the presented complexes and indeed the broader class of heteroleptic iridium(III) complexes to which they belong. A set of schematic potential energy surfaces are depicted in Figure 14 (except for compounds **3a–c** which only possess one emissive state) to summarize our interpretation of the data. In an attempt to classify the compounds in terms of their photophysical properties, we subdivide the Ir-emitters studied in this work into three classes.

For complexes **1a**, **2a**, and **2b** (Class I emitters, Figure 14), excitation from the ground state followed by rapid intersystem crossing results in selective population of the ^{3}MLCT/^{3}LC states with a rise time of 0.2 ps as inferred from TA data. In this case, we have assigned the decay time of 5–15 ps to the equilibration between the two ^{3}MLCT/^{3}LC states. **1a** and **2a–2b** are therefore phosphorescent from two equilibrated C^N-based states, an equilibrium which does not favor emission from the ancillary ligand-based state, both at room temperature and in frozen matrix where the N^N-based state is destabilized further. Hence, these complexes are actually quasi-dual emitters, but their two emissions are not resolved.

For **1c** and **2c** (Class III emitters), only a single C^N-based ^{3}MLCT/^{3}LC state can be located, and it is higher in energy than their N^N-based state. Transient absorption data reveal that this initial photoexcited ^{3}MLCT/^{3}LC state, rising in 0.1–

https://dx.doi.org/10.1021/acs.inorgchem.9b03003
Inorg. Chem. XXXX, XXX, XXX–XXX

0.2 ps, is rapidly depopulated in 1−2 ps and yields the vibrationally hot ^{3}MLCT/^{3}LL′CT state, subsequent vibrational relaxation of the latter requiring 20−25 ps. Only at cryogenic temperatures is an emission contribution from the ^{3}MLCT/^{3}LC state apparent; thus, these are quasi-dual emitters (very minor C^N-based contribution) until about 120 K. Rigid matrix effects enable the observation of the two emissions since it destabilizes the N^N-based state much more than the C^N-based state.

The most singular compound in this study is **1b** (Class II), which emerges as a particularly robust dual emitter over a broad range of temperatures and solvents. According to Watts and Crosby,[68−70] dual emission may be observed when two emissive states, almost isoenergetic and weakly coupled, produce two independent emissions.[59] Here, the initially populated ^{3}MLCT/^{3}LC states of **1b**, which appear in 0.15 ps, undergo rapid equilibration with, and partial population transfer to, the ^{3}MLCT/^{3}LL′CT state established in 12 ps, as indicated by transient absorption spectroscopy. This ensemble of states then gives rise to the observed dual emission character in steady state emission spectra. This unique combination causes the two radiative deactivation modes to be competitive, and remarkably, they remain so up to 60 °C.

CONCLUSION

A thorough experimental and theoretical survey of the photoluminescence characteristics of a series of heteroleptic biscyclometalated iridium(III) complexes has been reported. The results reveal modulation of the energies of the ^{3}MLCT/^{3}LC and ^{3}MLCT/^{3}LL′CT states through variation of the cyclometalated and ancillary ligands that enable selection of emission from one or other of these states and, importantly, for dual emission to be achieved as a result of radiative decay from both states. Ultrafast transient absorption spectroscopy has enabled us to identify spectral features that are highly characteristic of these two different key excited states, clearly allowing us to observe the occurrence of interligand energy transfer from initially populated ^{3}MLCT/^{3}LC states to ^{3}MLCT/^{3}LL′CT states. These transient excited-state spectral signatures further enable us to observe the equilibration between ^{3}MLCT/^{3}LC and ^{3}MLCT/^{3}LL′CT excited states where steady-state dual emission from both is evident.

In order to rationalize the observation of dual emission and energy transfer processes in the complexes reported, one needs to take into account the existence in some cases of two distinct C^N ligand-based ^{3}MLCT/^{3}LC states, as well as the effect at cryogenic temperatures of the rigid matrix on the relative energy of the N^N ancillary ligand-based ^{3}MLCT/^{3}LL′CT state. Changes to spectroscopic behavior between frozen glass and fluid solution are governed by the change in dipole moment between ground and excited states, leading here to a destabilization of the ^{3}MLCT/^{3}LL′CT state by the cryogenic rigid matrix.

Key structural changes between the ^{3}MLCT/^{3}LC and ^{3}MLCT/^{3}LL′CT states have been deciphered through computational calculations, suggesting that vibration of a Ir−N bond between the metal and N^N ancillary ligand principally mediates the ^{3}MLCT/^{3}LC−^{3}MLCT/^{3}LL′CT interconversion observed in **1b**, **1c**, and **2c** and allow us to provide fundamental mechanistic insights into the interligand energy transfer processes that these complexes undergo after photoexcitation. Further studies on well-established literature benchmark complexes are currently underway to assess the translation of these insights to a wider range of complexes. This work therefore provides illuminating insights into the fundamental photophysical properties of this industrially important class of phosphorescent complexes that represent a cornerstone of modern photophysics and photochemistry.

EXPERIMENTAL SECTION

General methods as well as synthetic descriptions for ligands and complexes are provided in the Supporting Information along with computational details.

ASSOCIATED CONTENT

Supporting Information

The Supporting Information is available free of charge at https://pubs.acs.org/doi/10.1021/acs.inorgchem.9b03003.

Experimental descriptions, synthesis of ligands and complexes, ^{1}H and ^{13}C NMR spectra and mass spectrometry data (Figures S1−S25), crystallographic data, transient absorption data for **2a−c**, computational details, spin densities, calculated absorption and emission spectra, analysis of vibrationally resolved emission spectra, and xyz coordinates for optimized minima (PDF)

Accession Codes

CCDC 1953486−1953488 contain the supplementary crystallographic data for this paper. These data can be obtained free of charge via www.ccdc.cam.ac.uk/data_request/cif, or by emailing data_request@ccdc.cam.ac.uk, or by contacting The Cambridge Crystallographic Data Centre, 12 Union Road, Cambridge CB2 1EZ, UK; fax: +44 1223 336033.

AUTHOR INFORMATION

Corresponding Authors

Paul A. Scattergood − *University of Huddersfield, Huddersfield, United Kingdom;* orcid.org/0000-0001-9070-5933; Email: p.a.scattergood@hud.ac.uk

Fabienne Alary − *Laboratoire de Chimie et Physique Quantiques, Toulouse, France;* orcid.org/0000-0003-4154-0815; Email: fabienne.alary@irsamc.ups-tlse.fr

Paul I. P. Elliott − *University of Huddersfield, Huddersfield, United Kingdom;* orcid.org/0000-0003-1570-3289; Email: p.i.elliott@hud.ac.uk

Other Authors

Anna M. Ranieri − *Curtin University, Bentley, Australia;* orcid.org/0000-0002-4612-2121

Luke Charalambou − *University of Huddersfield, Huddersfield, United Kingdom*

Adrian Comia − *University of Huddersfield, Huddersfield, United Kingdom*

Daniel A. W. Ross − *University of Huddersfield, Huddersfield, United Kingdom;* orcid.org/0000-0002-5480-9978

Craig R. Rice − *University of Huddersfield, Huddersfield, United Kingdom;* orcid.org/0000-0002-0630-4860

https://dx.doi.org/10.1021/acs.inorgchem.9b03003
Inorg. Chem. XXXX, XXX, XXX−XXX

Samantha J. O. Hardman − *The University of Manchester, Manchester, United Kingdom;* orcid.org/0000-0002-8310-4758
Jean-Louis Heully − *Laboratoire de Chimie et Physique Quantiques, Toulouse, France*
Isabelle M. Dixon − *Laboratoire de Chimie et Physique Quantiques, Toulouse, France;* orcid.org/0000-0001-5551-6715
Massimiliano Massi − *Curtin University, Bentley, Australia;* orcid.org/0000-0001-6949-4019

Complete contact information is available at: https://pubs.acs.org/10.1021/acs.inorgchem.9b03003

Notes

The authors declare no competing financial interest.

■ ACKNOWLEDGMENTS

We thank the University of Huddersfield (P.A.S, L.C., A.C., D.A.W.R., C.R.R., and P.I.P.E.) for supporting this work. The computational work performed in Toulouse used HPC resources from CALMIP (grant 2016-[p1112]) (I.M.D., J.-L.H., and F.A.). We also thank the Australian Research Council (grant LE130100052) and Curtin University for support (A.R. and M.M.). We thank Stephen Boyer at London Metropolitan University for carrying out the elemental microanalysis. This article is dedicated to Professor Robin Perutz FRS on the occasion of his 70th birthday.

■ REFERENCES

(1) Lai, P.-N.; Brysacz, C. H.; Alam, M. K.; Ayoub, N. A.; Gray, T. G.; Bao, J.; Teets, T. S. Highly Efficient Red-Emitting Bis-Cyclometalated Iridium Complexes. *J. Am. Chem. Soc.* **2018**, *140* (32), 10198−10207.
(2) Na, H.; Teets, T. S. Highly Luminescent Cyclometalated Iridium Complexes Generated by Nucleophilic Addition to Coordinated Isocyanides. *J. Am. Chem. Soc.* **2018**, *140* (20), 6353−6360.
(3) Baldo, M. A.; Thompson, M. E.; Forrest, S. R. High-efficiency fluorescent organic light-emitting devices using a phosphorescent sensitizer. *Nature* **2000**, *403* (6771), 750−753.
(4) Costa, R. D.; Ortí, E.; Bolink, H. J.; Graber, S.; Schaffner, S.; Neuburger, M.; Housecroft, C. E.; Constable, E. C. Archetype cationic iridium complexes and their use in solid-state light-emitting electrochemical cells. *Adv. Funct. Mater.* **2009**, *19* (21), 3456−3463.
(5) Costa, R. D.; Ortí, E.; Bolink, H. J.; Monti, F.; Accorsi, G.; Armaroli, N. Luminescent ionic transition-metal complexes for light-emitting electrochemical cells. *Angew. Chem., Int. Ed.* **2012**, *51* (33), 8178−8211.
(6) Ertl, C. D.; Momblona, C.; Pertegás, A.; Junquera-Hernández, J. M.; La-Placa, M.-G.; Prescimone, A.; Ortí, E.; Housecroft, C. E.; Constable, E. C.; Bolink, H. J. Highly Stable Red-Light-Emitting Electrochemical Cells. *J. Am. Chem. Soc.* **2017**, *139* (8), 3237−3248.
(7) King, S. M.; Claire, S.; Teixeira, R. I.; Dosumu, A. N.; Carrod, A. J.; Dehghani, H.; Hannon, M. J.; Ward, A. D.; Bicknell, R.; Botchway, S. W.; Hodges, N. J.; Pikramenou, Z. Iridium Nanoparticles for Multichannel Luminescence Lifetime Imaging, Mapping Localization in Live Cancer Cells. *J. Am. Chem. Soc.* **2018**, *140* (32), 10242−10249.
(8) Lo, K. K. W.; Louie, M. W.; Zhang, K. Y. Design of luminescent iridium(III) and rhenium(I) polypyridine complexes as in vitro and in vivo ion, molecular and biological probes. *Coord. Chem. Rev.* **2010**, *254* (21−22), 2603−2622.
(9) Yip, A. M. H.; Lo, K. K. W. Luminescent rhenium(I), ruthenium(II), and iridium(III) polypyridine complexes containing a poly(ethylene glycol) pendant or bioorthogonal reaction group as biological probes and photocytotoxic agents. *Coord. Chem. Rev.* **2018**, *361*, 138−163.
(10) Caporale, C.; Bader, C. A.; Sorvina, A.; MaGee, K. D. M.; Skelton, B. W.; Gillam, T. A.; Wright, P. J.; Raiteri, P.; Stagni, S.; Morrison, J. L.; Plush, S. E.; Brooks, D. A.; Massi, M. Investigating Intracellular Localisation and Cytotoxicity Trends for Neutral and Cationic Iridium Tetrazolato Complexes in Live Cells. *Chem. - Eur. J.* **2017**, *23* (62), 15666−15679.
(11) Caporale, C.; Massi, M. Cyclometalated iridium(III) complexes for life science. *Coord. Chem. Rev.* **2018**, *363*, 71−91.
(12) Sorvina, A.; Bader, C. A.; Darby, J. R. T.; Lock, M. C.; Soo, J. Y.; Johnson, I. R. D.; Caporale, C.; Voelcker, N. H.; Stagni, S.; Massi, M.; Morrison, J. L.; Plush, S. E.; Brooks, D. A. Mitochondrial imaging in live or fixed tissues using a luminescent iridium complex. *Sci. Rep.* **2018**, *8* (1), 8191.
(13) Tso, K. K. S.; Liu, H. W.; Lo, K. K. W. Phosphorogenic sensors for biothiols derived from cyclometalated iridium(III) polypyridine complexes containing a dinitrophenyl ether moiety. *J. Inorg. Biochem.* **2017**, *177*, 412−422.
(14) Guo, W.; Ding, H.; Gu, C.; Liu, Y.; Jiang, X.; Su, B.; Shao, Y. Potential-Resolved Multicolor Electrochemiluminescence for Multiplex Immunoassay in a Single Sample. *J. Am. Chem. Soc.* **2018**, *140* (46), 15904−15915.
(15) Nam, J. S.; Kang, M.-G.; Kang, J.; Park, S.-Y.; Lee, S. J. C.; Kim, H.-T.; Seo, J. K.; Kwon, O.-H.; Lim, M. H.; Rhee, H.-W.; Kwon, T.-H. Endoplasmic Reticulum-Localized Iridium(III) Complexes as Efficient Photodynamic Therapy Agents via Protein Modifications. *J. Am. Chem. Soc.* **2016**, *138* (34), 10968−10977.
(16) McKenzie, L. K.; Bryant, H. E.; Weinstein, J. A. Transition metal complexes as photosensitisers in one- and two-photon photodynamic therapy. *Coord. Chem. Rev.* **2019**, *379*, 2−29.
(17) Yi, S.; Lu, Z.; Zhang, J.; Wang, J.; Xie, Z.; Hou, L. Amphiphilic Gemini Iridium(III) Complex as a Mitochondria-Targeted Theranostic Agent for Tumor Imaging and Photodynamic Therapy. *ACS Appl. Mater. Interfaces* **2019**, *11* (17), 15276−15289.
(18) Skubi, K. L.; Kidd, J. B.; Jung, H.; Guzei, I. A.; Baik, M.-H.; Yoon, T. P. Enantioselective Excited-State Photoreactions Controlled by a Chiral Hydrogen-Bonding Iridium Sensitizer. *J. Am. Chem. Soc.* **2017**, *139* (47), 17186−17192.
(19) Curtin, P. N.; Tinker, L. L.; Burgess, C. M.; Cline, E. D.; Bernhard, S. Structure-activity correlations among iridium(III) photosensitizers in a robust water-reducing system. *Inorg. Chem.* **2009**, *48* (22), 10498−10506.
(20) Disalle, B. F.; Bernhard, S. Orchestrated photocatalytic water reduction using surface-adsorbing iridium photosensitizers. *J. Am. Chem. Soc.* **2011**, *133* (31), 11819−11821.
(21) McDaniel, N. D.; Coughlin, F. J.; Tinker, L. L.; Bernhard, S. Cyclometalated iridium(III) aquo complexes: Efficient and tunable catalysts for the homogeneous oxidation of water. *J. Am. Chem. Soc.* **2008**, *130* (1), 210−217.
(22) Tinker, L. L.; Bernhard, S. Photon-driven catalytic proton reduction with a robust homoleptic iridium(III) 6-phenyl-2,2′-bipyridine complex ($[Ir(C^N^N)_2]^+$). *Inorg. Chem.* **2009**, *48* (22), 10507−10511.
(23) Henwood, A. F.; Zysman-Colman, E. Lessons learned in tuning the optoelectronic properties of phosphorescent iridium(III) complexes. *Chem. Commun.* **2017**, *53* (5), 807−826.
(24) Colombo, M. G.; Brunold, T. C.; Riedener, T.; Güdel, H. U.; Förtsch, M.; Bürgi, H. B. Facial Tris Cyclometalated Rh^{3+} and Ir^{3+} Complexes: Their Synthesis, Structure, and Optical Spectroscopic Properties. *Inorg. Chem.* **1994**, *33* (3), 545−550.
(25) Ladouceur, S.; Zysman-Colman, E. A comprehensive survey of cationic Iridium(III) complexes bearing nontraditional ligand chelation motifs. *Eur. J. Inorg. Chem.* **2013**, *2013* (17), 2985−3007.
(26) Lamansky, S.; Djurovich, P.; Murphy, D.; Abdel-Razzaq, F.; Lee, H. E.; Adachi, C.; Burrows, P. E.; Forrest, S. R.; Thompson, M. E. Highly phosphorescent bis-cyclometalated iridium complexes: Synthesis, photophysical characterization, and use in organic light emitting diodes. *J. Am. Chem. Soc.* **2001**, *123* (18), 4304−4312.

(27) Maestri, M.; Sandrini, D.; Balzani, V.; von Zelewsky, A.; Deuschel-Cornioley, C.; Jolliet, P. Absorption Spectra and Luminescence Properties of Isomeric Platinum (II) and Palladium (II) Complexes containing 1,1′-biphenyldiyl, 2-phenylpyridine, and 2,2′-bipyridine as ligands. *Helv. Chim. Acta* **1988**, *71* (5), 1053−1059.
(28) Tschierlei, S.; Neubauer, A.; Rockstroh, N.; Karnahl, M.; Schwarzbach, P.; Junge, H.; Beller, M.; Lochbrunner, S. Ultrafast excited state dynamics of iridium(III) complexes and their changes upon immobilisation onto titanium dioxide layers. *Phys. Chem. Chem. Phys.* **2016**, *18* (16), 10682−10687.
(29) Pomarico, E.; Silatani, M.; Messina, F.; Braem, O.; Cannizzo, A.; Barranoff, E.; Klein, J. H.; Lambert, C.; Chergui, M. Dual luminescence, interligand decay, and nonradiative electronic relaxation of cyclometalated iridium complexes in solution. *J. Phys. Chem. C* **2016**, *120* (30), 16459−16469.
(30) Mydlak, M.; Bizzarri, C.; Hartmann, D.; Sarfert, W.; Schmid, G.; De Cola, L. Positively Charged Iridium(III) Triazole Derivatives as Blue Emitters for Light-Emitting Electrochemical Cells. *Adv. Funct. Mater.* **2010**, *20* (11), 1812−1820.
(31) Welby, C. E.; Gilmartin, L.; Marriott, R. R.; Zahid, A.; Rice, C. R.; Gibson, E. A.; Elliott, P. I. P. Luminescent biscyclometalated arylpyridine iridium(III) complexes with 4,4′-bi-1,2,3-triazolyl ancillary ligands. *Dalton Transactions* **2013**, *42* (37), 13527−13536.
(32) Felici, M.; Contreras-Carballada, P.; Smits, J. M. M.; Nolte, R. J. M.; Williams, R. M.; De Cola, L.; Feiters, M. C. Cationic Heteroleptic Cyclometalated Iridium (III) Complexes Containing Phenyl-Triazole and Triazole-Pyridine Clicked Ligands. *Molecules* **2010**, *15* (3), 2039−2059.
(33) Fernández-Hernández, J. M.; Ladouceur, S.; Shen, Y.; Iordache, A.; Wang, X.; Donato, L.; Gallagher-Duval, S.; de Anda Villa, M.; Slinker, J. D.; De Cola, L.; Zysman-Colman, E. Blue light emitting electrochemical cells incorporating triazole-based luminophores. *J. Mater. Chem. C* **2013**, *1* (44), 7440−7452.
(34) Suzuki, K.; Kobayashi, A.; Kaneko, S.; Takehira, K.; Yoshihara, T.; Ishida, H.; Shiina, Y.; Oishi, S.; Tobita, S. Reevaluation of absolute luminescence quantum yields of standard solutions using a spectrometer with an integrating sphere and a back-thinned CCD detector. *Phys. Chem. Chem. Phys.* **2009**, *11* (42), 9850−9860.
(35) Gitlina, A. Y.; Ivonina, M. V.; Sizov, V. V.; Starova, G. L.; Pushkarev, A. P.; Volyniuk, D.; Tunik, S. P.; Koshevoy, I. O.; Grachova, E. V. A rare example of a compact heteroleptic cyclometalated iridium(III) complex demonstrating well-separated dual emission. *Dalton Transactions* **2018**, *47* (22), 7578−7586.
(36) Kumar, S.; Hisamatsu, Y.; Tamaki, Y.; Ishitani, O.; Aoki, S. Design and Synthesis of Heteroleptic Cyclometalated Iridium(III) Complexes Containing Quinoline-Type Ligands that Exhibit Dual Phosphorescence. *Inorg. Chem.* **2016**, *55* (8), 3829−3843.
(37) Ladouceur, S.; Donato, L.; Romain, M.; Mudraboyina, B. P.; Johansen, M. B.; Wisner, J. A.; Zysman-Colman, E. A rare case of dual emission in a neutral heteroleptic iridium(III) complex. *Dalton Transactions* **2013**, *42* (24), 8838−8847.
(38) Lo, K. K. W.; Zhang, K. Y.; Leung, S. K.; Tang, M. C. Exploitation of the dual-emissive properties of cyclometalated iridium(III)-polypyridine complexes in the development of luminescent biological probes. *Angew. Chem., Int. Ed.* **2008**, *47* (12), 2213−2216.
(39) Yeh, Y. S.; Cheng, Y. M.; Chou, P. T.; Lee, G. H.; Yang, C. H.; Chi, Y.; Shu, C. F.; Wang, C. H. A new family of homoleptic Ir(III) complexes: Tris-pyridyl azolate derivatives with dual phosphorescence. *ChemPhysChem* **2006**, *7* (11), 2294−2297.
(40) Zhang, K. Y.; Liu, H. W.; Tang, M. C.; Choi, A. W. T.; Zhu, N.; Wei, X. G.; Lau, K. C.; Lo, K. K. W. Dual-Emissive Cyclometalated Iridium(III) Polypyridine Complexes as Ratiometric Biological Probes and Organelle-Selective Bioimaging Reagents. *Inorg. Chem.* **2015**, *54* (13), 6582−6593.
(41) You, Y.; Lee, S.; Kim, T.; Ohkubo, K.; Chae, W.-S.; Fukuzumi, S.; Jhon, G.-J.; Nam, W.; Lippard, S. J. Phosphorescent Sensor for Biological Mobile Zinc. *J. Am. Chem. Soc.* **2011**, *133* (45), 18328−18342.
(42) You, Y.; Han, Y.; Lee, Y.-M.; Park, S. Y.; Nam, W.; Lippard, S. J. Phosphorescent Sensor for Robust Quantification of Copper(II) Ion. *J. Am. Chem. Soc.* **2011**, *133* (30), 11488−11491.
(43) Zhang, K. Y.; Gao, P.; Sun, G.; Zhang, T.; Li, X.; Liu, S.; Zhao, Q.; Lo, K. K.-W.; Huang, W. Dual-Phosphorescent Iridium(III) Complexes Extending Oxygen Sensing from Hypoxia to Hyperoxia. *J. Am. Chem. Soc.* **2018**, *140* (25), 7827−7834.
(44) Sajoto, T.; Djurovich, P. I.; Tamayo, A. B.; Oxgaard, J.; Goddard, W. A.; Thompson, M. E. Temperature Dependence of Blue Phosphorescent Cyclometalated Ir(III) Complexes. *J. Am. Chem. Soc.* **2009**, *131* (28), 9813−9822.
(45) King, K. A.; Watts, R. J. Dual Emission from an Ortho-Metalated Ir(III) Complex. *J. Am. Chem. Soc.* **1987**, *109* (5), 1589−1590.
(46) Bevernaegie, R.; Marcélis, L.; Moreno-Betancourt, A.; Laramée-Milette, B.; Hanan, G. S.; Loiseau, F.; Sliwa, M.; Elias, B. Ultrafast charge transfer excited state dynamics in trifluoromethyl-substituted iridium(III) complexes. *Phys. Chem. Chem. Phys.* **2018**, *20* (43), 27256−27260.
(47) Cho, Y.-J.; Kim, S.-Y.; Son, H.-J.; Cho, D. W.; Kang, S. O. The effect of interligand energy transfer on the emission spectra of heteroleptic Ir complexes. *Phys. Chem. Chem. Phys.* **2017**, *19* (13), 8778−8786.
(48) Felici, M.; Contreras-Carballada, P.; Vida, Y.; Smits, J. M. M.; Nolte, R. J. M.; De Cola, L.; Williams, R. M.; Feiters, M. C. Ir (III) and Ru (II) Complexes Containing Triazole-Pyridine Ligands: Luminescence Enhancement upon Substitution with β-Cyclodextrin. *Chem. - Eur. J.* **2009**, *15* (47), 13124−13134.
(49) Wang, X.; Yang, H.; Wen, Y.; Wang, L.; Li, J.; Zhang, J. Comprehension of the Effect of a Hydroxyl Group in Ancillary Ligand on Phosphorescent Property for Heteroleptic Ir(III) Complexes: A Computational Study Using Quantitative Prediction. *Inorg. Chem.* **2017**, *56* (15), 8986−8995.
(50) Arroliga-Rocha, S.; Escudero, D. Facial and Meridional Isomers of Tris(bidentate) Ir(III) Complexes: Unravelling Their Different Excited State Reactivity. *Inorg. Chem.* **2018**, *57* (19), 12106−12112.
(51) Escudero, D.; Heuser, E.; Meier, R. J.; Schäferling, M.; Thiel, W.; Holder, E. Unveiling photodeactivation pathways for a new iridium(III) cyclometalated complex. *Chem. - Eur. J.* **2013**, *19* (46), 15639−15644.
(52) Zhou, X.; Burn, P. L.; Powell, B. J. Bond Fission and Non-Radiative Decay in Iridium(III) Complexes. *Inorg. Chem.* **2016**, *55* (11), 5266−5273.
(53) Treboux, G.; Mizukami, J.; Yabe, M.; Nakamura, S. Blue phosphorescent iridium(III) complex. A reaction path on the triplet potential energy surface. *Chem. Lett.* **2007**, *36* (11), 1344−1345.
(54) Zhou, X.; Powell, B. J. Nonradiative Decay and Stability of N-Heterocyclic Carbene Iridium(III) Complexes. *Inorg. Chem.* **2018**, *57* (15), 8881−8889.
(55) Baranoff, E.; Curchod, B. F. E. FIrpic: Archetypal blue phosphorescent emitter for electroluminescence. *Dalton Transactions* **2015**, *44* (18), 8318−8329.
(56) Baranoff, E.; Curchod, B. F. E.; Monti, F.; Steimer, F.; Accorsi, G.; Tavernelli, I.; Rothlisberger, U.; Scopelliti, R.; Grätzel, M.; Nazeeruddin, M. K. Influence of halogen atoms on a homologous series of bis-cyclometalated iridium(III) complexes. *Inorg. Chem.* **2012**, *51* (2), 799−811.
(57) Wang, Y.; Sun, N.; Curchod, B. F. E.; Male, L.; Ma, D.; Fan, J.; Liu, Y.; Zhu, W.; Baranoff, E. Tuning the oxidation potential of 2-phenylpyridine-based iridium complexes to improve the performance of bluish and white OLEDs. *J. Mater. Chem. C* **2016**, *4* (17), 3738−3746.
(58) Escudero, D. Mer-Ir(ppy)$_3$ to Fac-Ir(ppy)$_3$ Photoisomerization. *ChemPhotoChem.* **2019**, *3* (9), 697−701.
(59) Glazer, E. C.; Magde, D.; Tor, Y. Ruthenium Complexes That Break the Rules: Structural Features Controlling Dual Emission. *J. Am. Chem. Soc.* **2007**, *129* (27), 8544−8551.
(60) Chen, P.; Meyer, T. J. Electron Transfer in Frozen Media. *Inorg. Chem.* **1996**, *35* (19), 5520−5524.

https://dx.doi.org/10.1021/acs.inorgchem.9b03003
Inorg. Chem. XXXX, XXX, XXX−XXX

(61) Alary, F.; Heully, J. L.; Bijeire, L.; Vicendo, P. Is the ^{3}MLCT the only photoreactive state of polypyridyl complexes? *Inorg. Chem.* **2007**, *46* (8), 3154−3165.
(62) Henkelman, G.; Jóhannesson, G.; Jónsson, H. Methods for finding saddle points and minimum energy paths. *Progress in Theoretical Chemistry and Physics* **2002**, *5*, 269−302.
(63) Jónsson, H.; Mills, G.; Jacobsen, K. W. Nudged elastic band method for finding minimum energy paths of transitions. *Classical and Quantum Dynamics in Condensed Phase Simulations* **1997**, 385−404.
(64) Soupart, A.; Alary, F.; Heully, J. L.; Elliott, P. I. P.; Dixon, I. M. Exploration of Uncharted ^{3}PES Territory for $[Ru(bpy)_3]^{2+}$: A New ^{3}MC Minimum Prone to Ligand Loss Photochemistry. *Inorg. Chem.* **2018**, *57* (6), 3192−3196.
(65) Soupart, A.; Dixon, I. M.; Alary, F.; Heully, J. L. DFT rationalization of the room-temperature luminescence properties of $Ru(bpy)_3^{2+}$ and $Ru(tpy)_2^{2+}$: ^{3}MLCT−^{3}MC minimum energy path from NEB calculations and emission spectra from VRES calculations. *Theor. Chem. Acc.* **2018**, *137* (3), 37.
(66) Morris, D. E.; Hanck, K. W.; DeArmond, M. K. ESR studies of the redox orbitals in diimine complexes of iron(II) and ruthenium(II). *J. Am. Chem. Soc.* **1983**, *105* (10), 3032−3038.
(67) Moret, M.-E.; Tavernelli, I.; Chergui, M.; Rothlisberger, U. Electron Localization Dynamics in the Triplet Excited State of $[Ru(bpy)_3]^{2+}$ in Aqueous Solution. *Chem. - Eur. J.* **2010**, *16* (20), 5889−5894.
(68) Crosby, G. A.; Elfring, W. H. Excited states of mixed ligand chelates of ruthenium(II) and rhodium(III). *J. Phys. Chem.* **1976**, *80* (20), 2206−2211.
(69) Watts, R. J.; Griffith, B. G.; Harrington, J. S. The luminescence of heterobischelated complexes of iridium(III). II. Analysis of the thermally nonequilibrated levels in the luminescence of cis-dichloro-(1,10-phenanthroline)(4,7-dimethyl-1,10-phenanthroline)iridium-(III) chloride. *J. Am. Chem. Soc.* **1976**, *98* (3), 674−679.
(70) Watts, R. J.; Van Houten, J. The effect of energy gaps on multiple emissions in heterotrischelated rhodium(III) complexes. *J. Am. Chem. Soc.* **1978**, *100* (6), 1718−1721.

https://dx.doi.org/10.1021/acs.inorgchem.9b03003
Inorg. Chem. XXXX, XXX, XXX−XXX